ADVANCED FUNCTIONAL MATERIALS
www.afm-journal.de

Oral Dosed Organo-Silica Nanoparticles Restore Glucose Homeostasis and β-Cell Function in Diabetes Rats

Chenxiao Chu, Mingli Wei, Che Bian, Xiaoshuang Bi, Yaxin Deng, Peifu Xiao, Jiansong Zhao, Yuying Wang, Haibing He, Jingxin Gou, Tian Yin, Xing Tang, Li Yang, Hongbo Zhang,* and Yu Zhang**

Type 2 diabetes mellitus (T2DM) persists as a global health challenge, with current therapies inadequately addressing the intertwined pathologies of hyperglycemia, oxidative stress, and β-cell dysfunction. Here, an oral nanotherapeutic platform, MOP@T@D, engineered to restore glucose homeostasis and rejuvenate pancreatic β-cells is developed. The platform is constructed by co-loading insulin and glucose oxidase (GOx) into diselenide-bridged mesoporous organosilicon nanoparticles (MON), followed by sequential coating with transferrin (Tf) and functionalization with deoxycholic acid (Dc). MOP@T@D demonstrates efficient intestinal absorption and liver-targeted delivery, achieving an oral bioavailability of 10.6%. Under hyperglycemic conditions, GOx-generated H_2O_2 cleaves the diselenide bonds in the MON framework, resulting in rapid insulin release with 8.7-fold higher cumulative release compared to normoglycemic conditions. Simultaneously, the metabolized selenium derivatives progressively upregulate key selenoproteins, enhancing glutathione peroxidase (Gpx) activity by 31%, which effectively neutralizes oxidative stress and suppresses NF-κB-mediated inflammation. In a T2DM rat model, this therapy increases the islet area by 26.7% and restores insulin secretion to 74.6% of the physiological level. Notably, the system maintains normal blood glucose levels for two weeks after cessation of administration. In summary, through a simple oral dose, MOP@T@D not only stabilizes glycemic fluctuations but also addresses the root pathophysiology of T2DM.

1. Introduction

Diabetes mellitus has become a global health crisis, impacting over 528 million people worldwide. Type 2 diabetes mellitus (T2DM) accounts for more than 90% of all cases. Its pathogenesis stems from the complex interaction between insulin resistance and the gradual decline of β-cell function, resulting in persistent hyperglycemia and severe complications.[1] Although insulin therapy remains a cornerstone in the management of advanced T2DM, it often brings hypoglycemia risk and inevitable β-cell failure.[2,3]

Physiological glucose homeostasis relies on biphasic insulin secretion, consisting of a first-phase reverse response to nutrient intake and a subsequent sustained second-phase release to maintain peripheral glucose uptake.[4] Conventional exogenous insulin administration fails to replicate this dynamic secretory pattern. Moreover, it disrupts the natural physiological gradient from the portal vein to the periphery, leading to peripheral hyperinsulinemia while inadequately promoting hepatic glycogen storage.[5] Oral insulin delivery offers a

C. Chu, M. Wei, X. Bi, Y. Deng, P. Xiao, J. Zhao, Y. Wang, H. He, J. Gou, X. Tang, L. Yang, Y. Zhang
Department of Pharmaceutics
School of Pharmacy
Shenyang Pharmaceutical University
Shenyang 110016, China
E-mail: yangli@syphu.edu.cn; zhangyu@syphu.edu.cn

The ORCID identification number(s) for the author(s) of this article can be found under https://doi.org/10.1002/adfm.202519628

DOI: 10.1002/adfm.202519628

C. Bian
Department of Geriatrics
The Fourth Affiliated Hospital of China Medical University
Shenyang 110032, China

T. Yin
School of Chinese Materia Medica
Shenyang Pharmaceutical University
Shenyang 110016, China

H. Zhang
Pharmaceutical Sciences Laboratory
Åbo Akademi University
Turku 20520, Finland
E-mail: hongbo.zhang@abo.fi

H. Zhang
Turku Bioscience Centre
University of Turku and Åbo Akademi University
Turku 20520, Finland

promising alternative by utilizing the portal circulation to restore physiological insulin signaling pathways in the liver. However, its efficacy is limited by enzymatic degradation, low intestinal permeability, and a lack of glucose-responsive release, resulting in poor oral bioavailability.[6,7] Even the approved oral semaglutide formulation (Rybelsus) exhibits a bioavailability of less than 1%, highlighting the persistent challenges in this field.[8]

Although emerging nanotechnologies have shown potential for revolutionizing oral drug delivery, current platforms suffer from critical limitations. Most existing nanocarriers provide only passive or sustained drug release, lacking the dynamic glucose-responsive capability essential for mimicking physiological insulin secretion.[9,10] More importantly, conventional nanocarriers focus predominantly on drug delivery while overlooking the pathological oxidative microenvironment that perpetuates β-cell damage.[11,12] The hyperglycemia-driven reactive oxygen species (ROS) activate NF-κB-mediated inflammation pathways, creating a self-perpetuating cycle of β-cell loss and disease progression.[13] This represents a fundamental gap in current nanotherapeutic strategies for T2DM.

To address these limitations, we introduced MOP@T@D (MON-Proteins@Transferrin@Deoxycholic acid), an innovative oral nanotherapeutic platform engineered to address glucose homeostasis and β-cell regeneration (**Scheme 1**). MOP@T@D was fabricated by co-loading insulin and glucose oxidase (GOx) into mesoporous organosilicon nanoparticles (MON), followed by coating with transferrin (Tf) and subsequent functionalization with deoxycholic acid (Dc). The diselenide-bridged MON framework enabled glucose-responsive insulin release through glucose oxidase (GOx)-mediated H_2O_2 generation and subsequent diselenide bond cleavage.[14] The Tf-Dc functionalization ensured gastrointestinal stability and liver-targeted delivery,[15] achieving an oral bioavailability of 10.6%. Most notably, the metabolized selenium derivatives actively upregulated key antioxidant selenoproteins including glutathione peroxidase (Gpx), providing integrated antioxidant protection and anti-inflammatory effects that directly address the oxidative microenvironment driving β-cell dysfunction.[16,17] This multifunctional design represents a paradigm shift from conventional nanocarriers by simultaneously enabling intelligent glucose-responsive drug release and active modification of core disease pathophysiology.

2. Results and Discussion

2.1. Preparation and Characterization of Glucose-Responsive Carriers

2.1.1. Structural and Morphology Validation of Diselenide-Bridged MON

To enable environmental responsiveness insulin release, we prepared mesoporous organosilica nanoparticles (MON) by integrating dynamic diselenide (Se—Se) bonds into the silica framework.[18] Here, we first synthesized H_2O_2-sensitive diselenide-bridged organo-silica precursor, bis [3-(triethoxysiliconyl) propyl] diselenide (BTESePD) and confirmed the successful synthesizing by MS (Figure S1, Supporting Information), ^{1}H NMR (Figure S2, Supporting Information), and ^{13}C NMR (Figure S3, Supporting Information). Notably, an upfield shift of the β-hydrogens in BTESePD, compared to its precursor γ-chloropropyl trimethoxysilane (CP), stems from the reduced electron-withdrawing inductive effect following chlorine substitution with a diselenide moiety. Subsequently, MON was fabricated via a sol–gel method using the synthesized BTESePD precursor (**Figure 1a**). For comparison, non-responsive control nanoparticles (MSN) were synthesized under identical conditions using a carbon-bridged precursor, 1,6-bis(triethoxysilyl)hexane (BTESiH) (Figure S4a, Supporting Information).

Dynamic light scattering (DLS) analysis indicated that MON nanoparticles had a mean size of 90.3 nm and a positive charge (+15.5 mV) (Figure 1b). The spherical and homogeneous shape of MON was further verified using transmission electron microscopy (TEM) (Figure 1c). Nitrogen adsorption–desorption isotherms for both MON and MSN displayed typical Type IV profiles (Figure S4b, Supporting Information), characteristic of mesoporous materials. Based on Brunauer–Emmett–Teller (BET) analysis, the specific surface area of MON was calculated to be 386.6 m^2 g^{-1}, with an average pore diameter of 9.2 nm, values closely comparable to those of MSN (359.2 m^2 g^{-1} and 8.7 nm, respectively). This large pore size was conducive to drug loading without compromising structural integrity. The presence of diselenide bonds in the MON skeleton was indicated by Fourier transform infrared (FTIR) spectroscopy, which showed a characteristic absorption band in the range of 550–750 cm^{-1} (Figure 1d)—a feature absent in the FTIR spectrum of MSN (Figure S4c, Supporting Information). Furthermore, X-ray photoelectron spectroscopy (XPS) analysis validated the existence of diselenide bonds through distinct Se 3^d peaks (Figure 1e).

2.1.2. Preparation and Characterization of Functionalized Blank Carrier (MON@T@D)

To verify the synthesis process, the blank MON nanoparticles were prepared by sequentially coating with transferrin (Tf) and functionalization with deoxycholic acid (Dc) to obtain MON@T@D. MSN@T@D was prepared similarly as a control. DLS analysis showed that Tf coating increased the hydrodynamic diameter of MON to 136.6 ± 16 nm and shifted the zeta potential to 24.1 ± 3.1 mV (Figure 1b). Subsequent functionalization with Dc reduced both the particle size (120.1 ± 3.2 nm) and zeta potential (3.2 ± 1.5 mV) of MON@T@D, consistent with effective charge screening and steric stabilization conferred by Dc. TEM revealed that MON@T@D exhibited a uniform spherical morphology with obscured mesopores, contrasting with the well-defined porous structure of unmodified MON (Figure 1c). FTIR spectroscopy further confirmed the presence of Tf, as evidenced by characteristic amide I bands at 1652 and 1560 cm^{-1} (Figure 1d). Fluorescence resonance energy transfer (FRET) analysis between FITC-labeled MON and RITC-labeled Tf demonstrated efficient energy transfer with an efficiency of 34%, corroborating the successful grafting of Tf on the MON surface (Figure 1f). Moreover, energy dispersive X-ray spectroscopy (EDS) elemental mapping further demonstrated a uniform distribution of Si and Se (from BTESePD), and Fe, N, and O (from Tf and Dc) (Figure 1g,h), corroborating the successful surface modification of the blank carrier.

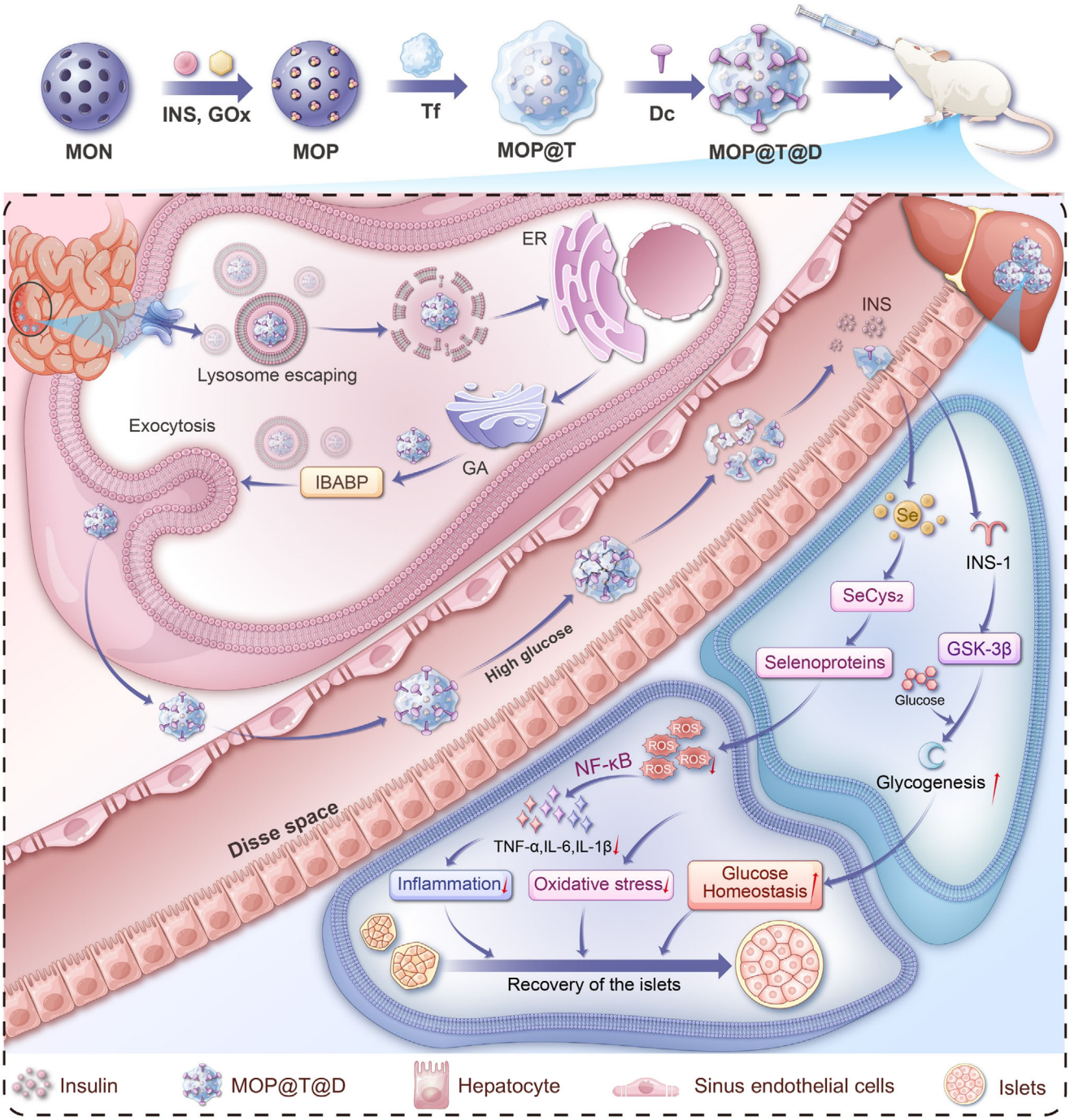

Scheme 1. Schematic illustration of MOP@T@D for efficient oral insulin delivery, intelligent blood glucose regulation, and eventual recovery of islet β-cell function.

2.1.3. Preparation and Characterization of Insulin/GOx-Coloaded Nanoparticles (MOP@T@D)

The therapeutic nanoparticles (MON-payload@T@D, abbreviated as MOP@T@D) were fabricated by co-loading insulin and GOx into MON nanoparticles, followed by surface coating with transferrin and subsequent functionalization with deoxycholic acid, as illustrated in Figure 1i. MOP@T@D exhibited a hydrodynamic diameter of 121.7 ± 9.24 nm and a zeta potential of 4.2 ± 1.31 mV (Figure S5, Supporting Information). The negligible change in the hydrodynamic diameter of MOP@T@D compared to blank MON@T@D indicated that the payload was primarily encapsulated within the mesopores without inducing significant aggregation or surface attachment, which was consistent with efficient pore loading. Successful encapsulation of insulin was further verified by the FRET phenomenon using

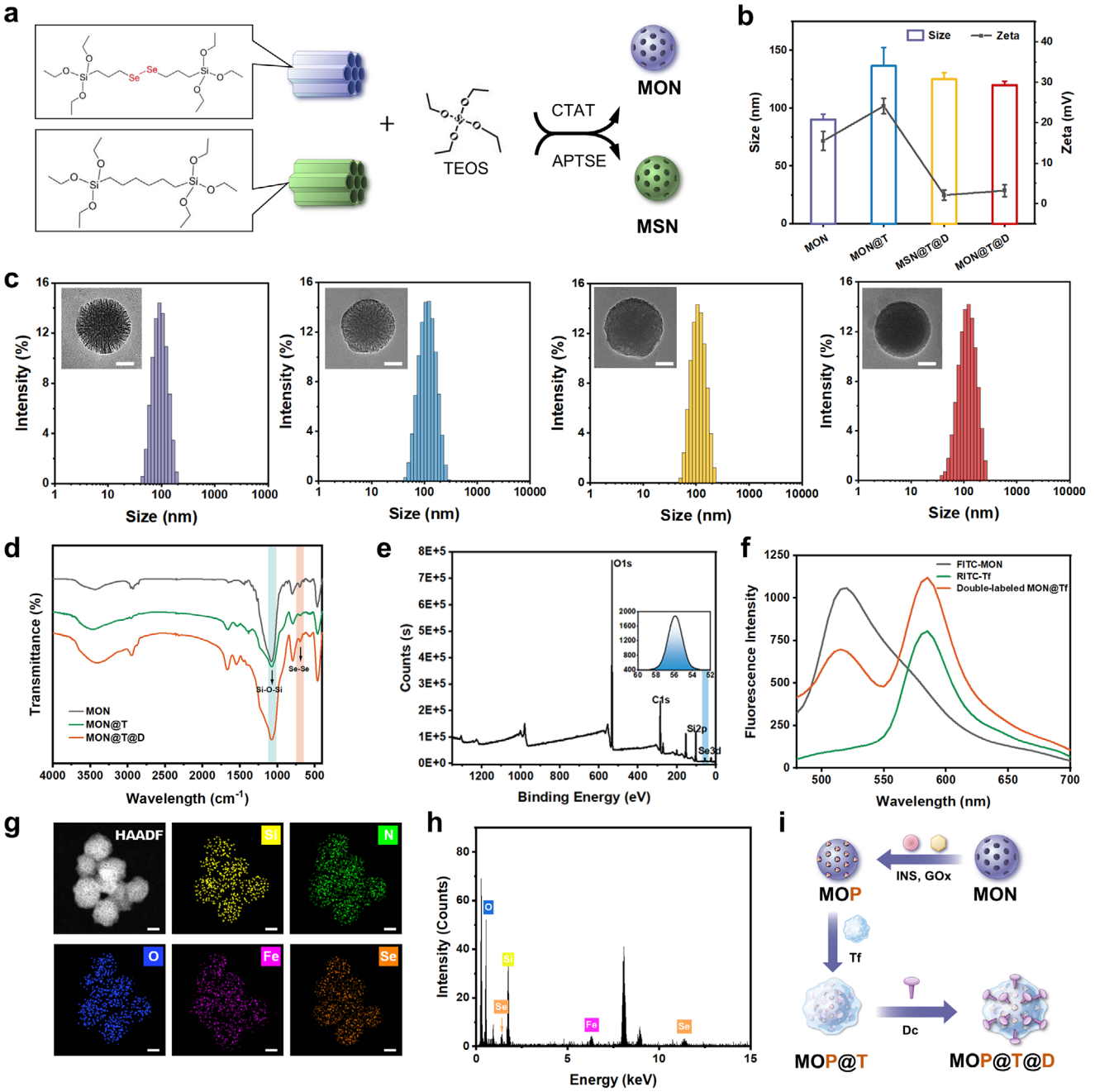

Figure 1. Synthesis and characterization of glucose-responsive carriers. a) Schematic illustration of MSN and MON by the modified sol–gel method. b) Size and zeta potential of MON, MON@T, MSN@T@D and MON@T@D ($n = 3$). c) Size distributions and representative TEM images of MON, MON@T, MSN@T@D, and MON@T@D ($n = 3$). Scale bar: 30 nm. d) FTIR spectrum of MON, MON@T, and MON@T@D ($n = 3$). e) XPS analysis of Se 3^d binding energy of MON ($n = 3$). f) Emission spectra of FITC-MON, RITC-Tf, and dual-labeled MON@T at an excitation at 425 nm ($n = 3$). g) HAADF-STEM image of MOP@T@D, along with the corresponding EDS element maps of Si, N, O, Fe, and Se. Scale bar: 30 nm. h) EDS spectra of MOP@T@D ($n = 3$). i) Schematic diagram of the preparation process of MOP@T@D loading with insulin and GOx. Data presented as means ± SD.

FITC-labeled insulin and RITC-labeled MON within the MOP@T@D structure (Figure S6, Supporting Information).

The loading mechanism relied on the electrostatic attraction between the proteins and the nanoparticle pores. Since insulin and GOx have isoelectric points ≈5.3 and 4.2, respectively, both proteins carried a net negative charge under the preparation conditions (PBS, pH 7.4). This negative charge facilitated their attraction and retention within the positively charged pores. A 12-h stirring period ensured complete diffusion and efficient loading, followed by repeated centrifugal washing to remove most superficially adsorbed molecules. The subsequent Tf coating acted as a sealing layer over the pore openings, thereby

minimizing premature payload release and further securing the loaded proteins.

The loading content of insulin and GOx was determined by quantifying the unencapsulated proteins in the supernatant of the crude MOP nanoparticles. The loading content reached 29.2 wt.% for insulin and 8.2 wt.% for GOx. For comparison, the control nanoparticles (MSP@T@D) exhibited comparable loading contents of 27.8 wt.% for insulin and 7.9 wt.% for GOx.

2.2. Glucose-Responsive Insulin Release via Diselenide Bond Cleavage

2.2.1. H_2O_2-Triggered Diselenide Bond Cleavage Enabled On-Demand Insulin Release

Conventional insulin therapies lack dynamic responsiveness to glycemic fluctuations, often leading to hypoglycemia and suboptimal glucose control.[19,20] To address this limitation, MOP@T@D was designed to release insulin on-demand in response to hyperglycemia. Under high glucose conditions, GOx encapsulated within the MON@T@D nanoparticles catalyzed the oxidation of glucose, leading to localized H_2O_2 generation.[21] The resulting H_2O_2 can induce the cleavage of the diselenide bond to trigger the MON degradation, thus facilitating the subsequent release of insulin in a glucose-responsive manner. The sensitivity of MON@T@D to exogenous H_2O_2 was first verified. Size distribution analysis revealed a concentration-dependent dissociation of MON, with significant fragmentation observed at 100 μM H_2O_2 (Figure S7a, Supporting Information). The release rate of insulin from MOP@T@D also showed a gradient change with the increase of H_2O_2 concentration (Figure S7b, Supporting Information), demonstrating precise H_2O_2-sensitive release kinetics.

2.2.2. Glucose-Responsive Insulin Release Mimicking Physiological Dynamics

Next, we evaluated the glucose-dependent degradation profile of MOP@T@D. At a low glucose level (100 mg dL^{-1}), the particle size of MOP@T@D remained nearly unchanged (**Figure 2a**). In contrast, under high glucose conditions (400 mg dL^{-1}), a marked size increase and broader size distribution were observed (Figure 2b). This structural disruption was further evidenced by FRET analysis, which revealed sustained signal intensity under low glucose conditions (Figure 2c), in stark contrast to the pronounced reduction in signal intensity observed under high glucose stimulation (Figure 2d). These results confirmed that MOP@T@D remained stable under normoglycemic conditions (Figure 2e), while undergoing selective degradation in a hyperglycemic microenvironment (Figure 2f). After 72 h incubation in high glucose, TEM revealed complete disintegration of MOP@T@D into fragmented structures (Figure 2g), while control nanoparticles (MSP@T@D) and PBS-treated MOP@T@D maintained structural integrity (Figure S8, Supporting Information). XPS analysis confirmed the degradation mechanism through a characteristic shift in Se 3^d binding energy from 56 to 60 eV (Figure 2h), indicating diselenide bond cleavage and oxidation to selenic acid.

The insulin release profiles from MOP@T@D under fluctuating glucose concentrations were evaluated. Under normoglycemia (100 mg dL^{-1}), insulin release remained minimal (<15% within 12 h), while hyperglycemia (400 mg dL^{-1}) accelerated release rates by 3.2-fold (Figure 2i). To simulate postprandial glucose fluctuations, we cycled the environment between low and high glucose. This resulted in a pulsatile insulin release pattern (Figure 2j; Figure S9, Supporting Information), closely resembling the natural secretion rhythm of pancreatic β-cells. Importantly, insulin release stopped when glucose levels returned to normal, as the diselenide bonds remained stable under these conditions. Different degrees of hyperglycemia would induce different rates of insulin release, which ensured the precise control of insulin release.

It is also important to note that GOx remained securely encapsulated inside MOP@T@D under both PBS and high glucose conditions, ensuring sustained enzymatic functionality (Figure S10a, Supporting Information). We also measured H_2O_2 levels in MSP@T@D and MOP@T@D under both PBS and high glucose conditions. MSP@T@D showed significantly elevated H_2O_2 under hyperglycemia, while MOP@T@D maintained minimal H_2O_2 leakage, comparable to PBS controls (Figure S10b, Supporting Information). This inhibitory effect occurred because the H_2O_2 produced enzymatically was immediately consumed in cleaving the diselenide bond to trigger responsive insulin release. Virtually no additional H_2O_2 leakage effectively avoided the potential possibility of oxidative damage to surrounding tissues.

2.2.3. Structural Stability and Bioactivity in Simulated Gastrointestinal Tract

For oral delivery of biopharmaceuticals, stability under gastrointestinal conditions was paramount. MOP@T@D was exposed to sequential incubation in simulated gastric fluid (SGF, 2 h) and simulated intestinal fluid (SIF, 6 h) to mimic physiological transit. MOP@T@D exhibited outstanding stability in both SGF (Figure S11b, Supporting Information) and SIF (Figure S11b, Supporting Information), as well as in 3 mM bile salts (Figure S11c, Supporting Information), which was crucial for ensuring intact delivery to the intestinal absorption site. The insulin release under these conditions remained minimal, with cumulative leakage below 11% over 8 h (Figure 2k). This effective retention contributed to the spatial confinement offered by the mesoporous framework and the sealing effect of transferrin coating on the pore openings.[22]

The structural and functional integrity of the encapsulated insulin was also verified. Circular dichroism spectroscopy confirmed that insulin released from MOP@T@D retained its native α-helical secondary structure (Figure S12, Supporting Information). Furthermore, in vivo bioactivity assessed via subcutaneous injection showed glucose-lowering efficacy equivalent to that of native insulin (Figure S13, Supporting Information). Collectively, these results underscored the ability of MOP@T@D to preserve insulin structure and bioactivity throughout the gastrointestinal environment, highlighting its potential as a reliable oral delivery platform.

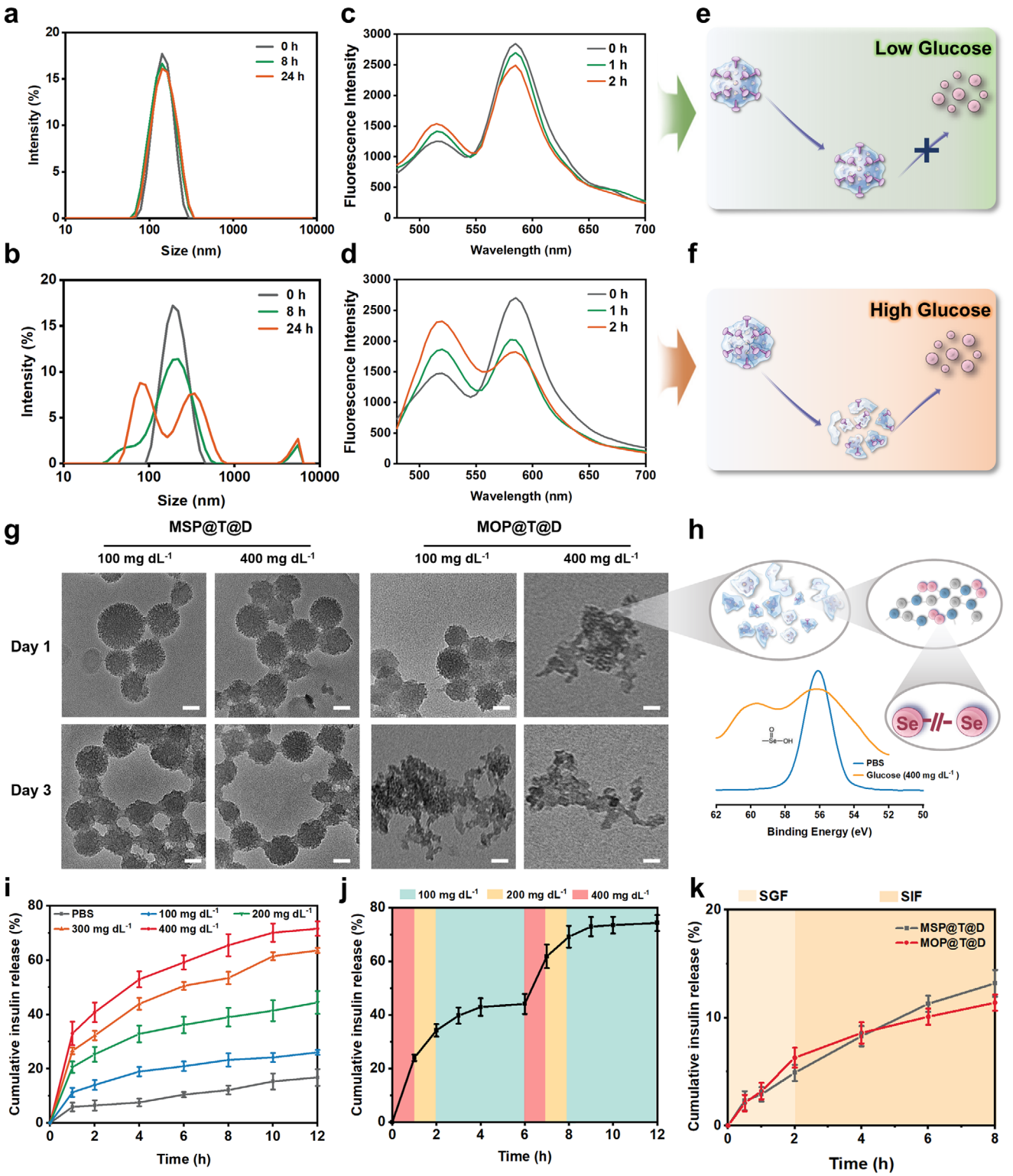

Figure 2. Glucose-responsive insulin release of MOP@T@D. Size analysis of MOP@T@D in a) 100 mg dL^{-1} (low) and b) 400 mg dL^{-1} (high) glucose conditions, respectively ($n = 3$). Emission spectra of dual-fluorescent-labeled MOP@T@D within c) 100 and d) 400 mg dL^{-1} glucose conditions (425 nm) ($n = 3$). Schematic diagram of MOP@T@D release under e) low and f) high glucose conditions. g) TEM images of MOP@T@D and MSP@T@D with low and high glucose conditions at 37 °C for 24 and 72 h ($n = 3$). Scale bars: 50 nm. h) XPS analysis of Se 3^d binding energy in MON after incubation in PBS and high glucose conditions ($n = 3$). i) Release profiles of MOP@T@D at various glucose conditions at 37 °C ($n = 3$). j) Insulin release profile of MOP@T@D in repeated high/medium/low glucose cycles ($n = 3$). k) Continuous release of insulin from MOP@T@D under SGF and SIF ($n = 3$). Data presented as means ± SD.

2.3. Mucus Penetration and Cellular Uptake

2.3.1. Neutral Surface Properties Overcame the Mucus Barrier

The mucus layer is one of the important barriers for oral absorption of nanocarriers. To evaluate mucus permeation, we employed freshly obtained porcine small intestinal mucus. Nanoparticle tracking analysis showed that the mobility of MOP@T@D showed a considerable range compared to MOP and MOP@T (**Figure** 3a). The mean squared displacement (MSD), which quantifies nanoparticle diffusion dynamics in mucus, showed a positive correlation with mucus diffusion rates. At a 1-second time interval, the MSD of MOP@T@D was 19.8 times higher than that of MOP@T (Figure 3b). In addition, a Transwell permeable scaffold was utilized to construct a 3D mucus model. The quantification of the transport rate was accomplished through the apparent permeability coefficient (Papp) value. The Papp value of MOP@T was slightly lower than that of MOP, consistent with the trend observed between MSP@T and MSP (Figure S14, Supporting Information). This reduction could be attributed to the strong positive charge of MOP@T, which enhanced the electrostatic interaction with negatively charged mucin. In contrast, Dc modification conferred a neutral surface to MOP@T@D, with the permeation ability increasing by 63.1% compared to MOP and 74% compared to MOP@T (Figure 3c).

The mucin penetration depth of nanoparticles was based on the HT29-MTX-E12 monolayer model that secretes mucin (Figure 3d). MOP@T@D penetrated deeply and aggregated at the bottom (0-140 nm) within 2 h, outperforming MSP, MOP, MSP@T, and MOP@T (Figure 3e; Figure S15, Supporting Information). The neutral charge property of MOP@T@D minimized the electrostatic interaction with mucin. Additionally, charge neutralization reduced the thickness of the hydration layer, resulting in a smaller hydrodynamic diameter, which also contributed to improved mucus penetration.

2.3.2. Overcoming the Apical Membrane Barrier via Dc-Mediated Uptake

Cytotoxicity data indicated that all formulations were nontoxic to Caco-2 and HT29-MTX-E12 cells at concentrations of 0.1–1 mg mL^{-1} (Figure S16, Supporting Information). Cellular uptake of FITC-INS-loaded nanoparticles was measured by a Caco-2 cell monolayer. MOP@T displayed a 2.1-fold higher uptake compared to MOP (Figure 3f; Figure S17, Supporting Information), which could be attributed to the presence of transferrin transporters on epithelial cells. Nevertheless, the overall uptake of MOP@T remained limited. The positively charged surface of MOP@T may facilitate nonspecific charge-mediated endocytosis; however, this mechanism alone appeared insufficient for efficient cellular internalization. In contrast, Dc-modified MOP@T@D showed markedly enhanced endocytosis, with uptake efficiencies being 4.5-fold and 1.7-fold that of MOP and MOP@T, respectively, underscoring the critical role of Dc in promoting epithelial internalization.[23]

To elucidate the uptake mechanism of MOP@T@D, competitive inhibition assays were performed using free Tf and Dc (Figure 3g). The cellular uptake of MOP@T@D decreased by 23% and 75.4% in the presence of Tf and Dc, respectively (Figure 3h), indicating that Dc mediated the dominant pathway for uptake. Although the steric hindrance from deoxycholic acid impaired direct interaction between the transferrin coating and its receptor, the exposed deoxycholic acid promoted cellular internalization of the MOP@T@D nanoparticles through the apical sodium-dependent bile acid transporter (ASBT).[24] The confocal microscopy further revealed extensive co-localization of MOP@T@D (green) with ASBT (red) at the cytoplasmic membrane, whereas MOP@T showed negligible overlap (Figure 3i). These results collectively confirmed that Dc potently enhanced the cellular uptake of MOP@T@D through an ASBT-dependent pathway, effectively utilizing the physiological bile acid absorption route.

2.3.3. Lysosomal Escape and ER-Golgi Trafficking Facilitated Transcellular Transport

The in vivo epithelium consists of multiple cell types functioning in concert. To better mimic this physiological complexity, we established an intestinal barrier model using a co-culture of Caco-2 and HT29-MTX-E12 cells at a 9:1 ratio. This system incorporated both the absorptive function of enterocytes (Caco-2 cell) and the protective mucus secretion of goblet-like cells (HT29-MTX-E12 cell),[25] thereby providing a more physiologically relevant platform for assessing peptide permeability and absorption than monocultures alone. To verify the integrity of the barrier, the transepithelial electrical resistance (TEER) was monitored over the 21-day culture period. TEER values increased progressively and stabilized at 1000–1200 $\Omega \times cm^2$ by day 21 (Figure S18, Supporting Information), indicating that tight junctions were successfully formed and were suitable for subsequent permeability studies.

The apical membrane barrier does not represent the last barrier; most carriers would face the dilemma of "easy entry, hard transcytosis". After incubation with Caco-2 monolayer (without mucus), the Papp value of MOP@T@D was 8.5 times and 2.9 times higher than that of insulin solution and MOP@T, respectively (Figure 3j; Figure S19, Supporting Information), indicating that Dc modification significantly enhanced the transcytosis of nanoparticles. However, when tested in a co-incubation model with Caco-2/HT29-MTX-E12 cells (with mucus), the Papp of MOP@T was significantly reduced. This reduction was attributed to the electrostatic interaction between positively charged MOP@T and negatively charged mucins in the mucus, which led to the retention of nanoparticles and restricted their mucus penetration.

To verify that transport occurred via a transcellular route, we monitored TEER and tight junction integrity. The TEER values stayed stable during the transport assay (Figure S20a, Supporting Information). Consistent with this, occluding immunostaining revealed intact tight junctions after 2 h of exposure to insulin and MOP@T@D (Figure S20b, Supporting Information). This indicated that MOP@T@D penetrated the cell layer through transcellular transport without disrupting the integrity of tight junctions, thereby minimizing the risk of pathogen infiltration or inflammation associated with paracellular leakage.

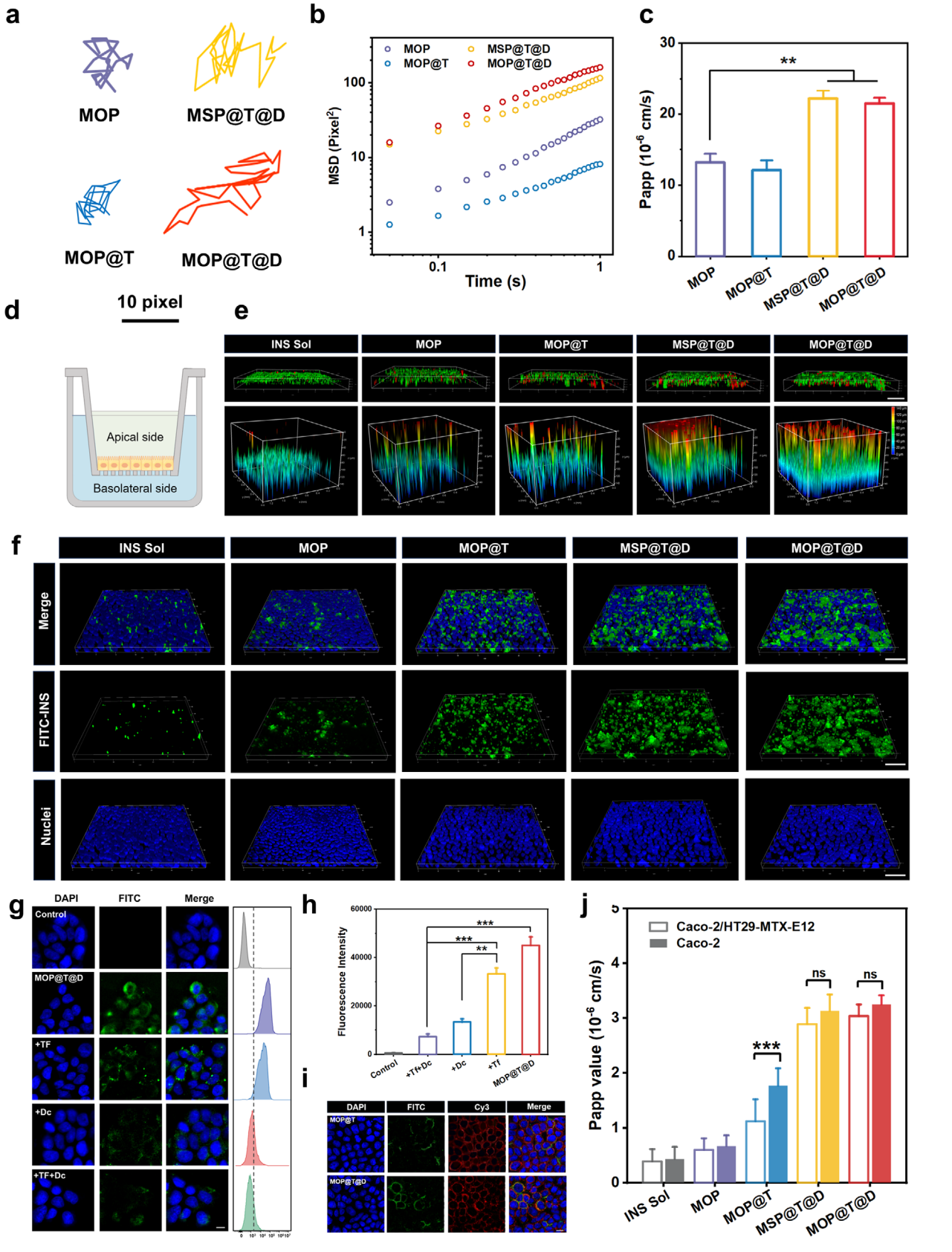

Based on these findings, we further investigated the intracellular transport pathways of MOP@T@D. Post-uptake, nanoparticles often face lysosomal entrapment, which is a critical bottleneck for oral delivery. Initially, at 0.5 h post-incubation, all formulations showed comparable lysosomal colocalization (**Figure 4a**). However, by 2 h, MOP@T@D exhibited significantly reduced Pearson's colocalization coefficient with lysosomes (Figure 4c), corresponding to a lysosomal escape efficiency of 68%. This efficiency significantly exceeded those of MOP (8%) and MOP@T (46%). This enhanced escape was likely mediated by the membrane-disruptive property of Dc, which could destabilize lysosomal membranes by disrupting lipid microdomains.[26]

After escaping lysosomes, MOP@T@D was efficiently trafficked to the endoplasmic reticulum (ER) and Golgi apparatus (Figure 4b), as evidenced by $P_{ER} = 0.51$ (Figure 4d) and $P_{Golgi} = 0.66$ (Figure 4e). While positively charged carriers such as MOP@T may inherently localize to these organelles,[27] the higher ER and Golgi association observed for MOP@T@D and MSP@T@D was likely a consequence of their superior lysosomal escape efficiency, which facilitated subsequent access to the secretory organelles and promotes transcellular transport.

2.3.4. MOP@T@D Traversed the Basolateral Membrane in an Intact State

Next, whether MOP@T@D completed the basolateral exocytosis in a complete form was subsequently studied. MOP@T@D was prepared using INS-FITC and MON-RITC and co-incubated with Caco-2 monolayers for 2 h. The collected basolateral medium showed a strong FRET signal, confirming that the nanoparticles remained structurally integrated during transcellular transport (Figure S21, Supporting Information). MOP@T@D was also visible in the basolateral culture medium by cryo-transmission electron microscopy.

Given that the cytosolic ileal bile acid-binding protein (IBABP) facilitated the systemic entry of deoxycholic acid, we examined whether it also participated in the transport of MOP@T@D. CLSM confirmed strong co-localization of MOP@T@D with IBABP (Figure 4f), indicating that IBABP participated in the basolateral exocytosis of nanoparticles. Taken together, these results supported an "easy entry, easy exit" transport pathway. Specifically, MOP@T@D entered enterocytes via ASBT-mediated uptake, followed by lysosomal escape, ER-Golgi trafficking, and IBABP-assisted systemic entry (Figure 4g). This coordinated process enabled the efficient transcellular delivery of intact MOP@T@D.

2.4. MOP@T@D Achieved Effective Hepatic Biodistribution after Intestinal Permeability

After modifying deoxycholic acid, MOP@T@D had an electrically neutral surface, which minimized adverse electrostatic interference. This property prevented the nanoparticles from being trapped by negatively charged mucoproteins or repelled by the anionic cell membrane, which was a prerequisite for all subsequent uptake by epithelial cells. In situ confocal imaging of rat ileal slices revealed that double-labeled MOP@T@D successfully escaped from mucus—unlike cationic MOP@T counterparts—and were subsequently absorbed by the villi (**Figure 5a**; Figure S22, Supporting Information). This "mucus-evading, epithelium-targeting" behavior underscored the critical role of MOP@T@D in transcellular transport, enabling intact nanoparticles (indicated by yellow fluorescence) to traverse the mucosal and epithelial barrier. The ex vivo permeability of nanoparticles in duodenal, jejunal, and ileal tissues was further evaluated. MOP@T@D exhibited superior ileal permeability despite of the thicker mucus layer (480 ± 47 vs 170 ± 38 μm in duodenum; Figure 5b; Figure S23, Supporting Information), attributing to ileum-specific overexpression of ASBT.[28] These findings confirmed the comprehensive intestinal permeability of MOP@T@D, characterized by significant mucus penetration and transcellular transport.

In addition, we performed in vivo imaging (IVIS) in Sprague–Dawley (SD) rats 4 h after oral administration of FITC-insulin-labeled formulations. Deoxycholic acid-functionalized nanoparticles (MSP@T@D and MOP@T@D) exhibited pronounced fluorescence signals specifically in the liver, which were significantly stronger than those in other organs. More importantly, the semi-quantitative analysis revealed that the fluorescence intensity of MOP@T@D in the liver was 7.1 times and 4.3 times that of the MOP group and the MOP@T group, respectively (Figure 5c,d). These results demonstrated that deoxycholic acid functionalization was responsible for the enhanced hepatotropic targeting. This liver-targeted behavior simulated the physiological pathway of insulin transport through the portal vein and was conducive to the direct regulation of glucose metabolism for insulin in the liver.

2.5. MOP@T@D Exerted Glucose-Response Insulin Release Advantage in the Liver

Mimicking natural insulin action necessitates both efficient delivery of insulin carriers to the liver and a glucose-responsive release mechanism.[29] In healthy rats, strong co-localization fluorescence (yellow) in healthy rat liver tissue indicated the accumulation of intact MOP@T@D nanoparticles (Figure 5e). In

Figure 3. Evaluation of mucus penetration and cellular uptake of nanoparticles. a) Representative trajectory of nanoparticles in 1 s within porcine mucus ($n = 3$). Scale bar: 10 pixels. b) Mean square displacement results of nanoparticles ($n = 3$). c) Permeability analysis of nanoparticles in 3D mucus system ($n = 3$). d) Schematic diagram of the cell monolayer model. e) 3D images (up) and mucus penetration depth maps (down) of Cy5-INS-loaded nanoparticles in HT29-MTX-E12 cells within 0–140 nm ($n = 3$). Mucus was labeled with Alexa 488-WGA (green). Scale bar: 100 μm. f) 3D images of Caco-2 monolayers after incubated with FITC-INS-loaded nanoparticles for 4 h ($n = 3$). Scale bar: 50 μm. Cellular uptake of MOP@T@D in monolayers pre-treated with Tf or Dc and analyzed via g) CLSM and h) Flow cytometry ($n = 3$). Scale bar: 20 μm. i) Fluorescence co-localization analysis of ASBT and MOP@T or MOP@T@D (red: Cy3-labeled ASBT antibody, green: FITC-INS-loaded nanoparticles) ($n = 3$). Scale bar: 10 μm. j) Papp values of nanoparticles transported across the Caco-2/HT29-MTX-E12 monolayers in Transwell ($n = 3$). Data presented as means ± SD. Statistical analysis was performed using one-way ANOVA with Tukey's multiple comparisons test. $^*P < 0.05$; $^{**}P < 0.01$; $^{***}P < 0.001$; ns, no significant difference.

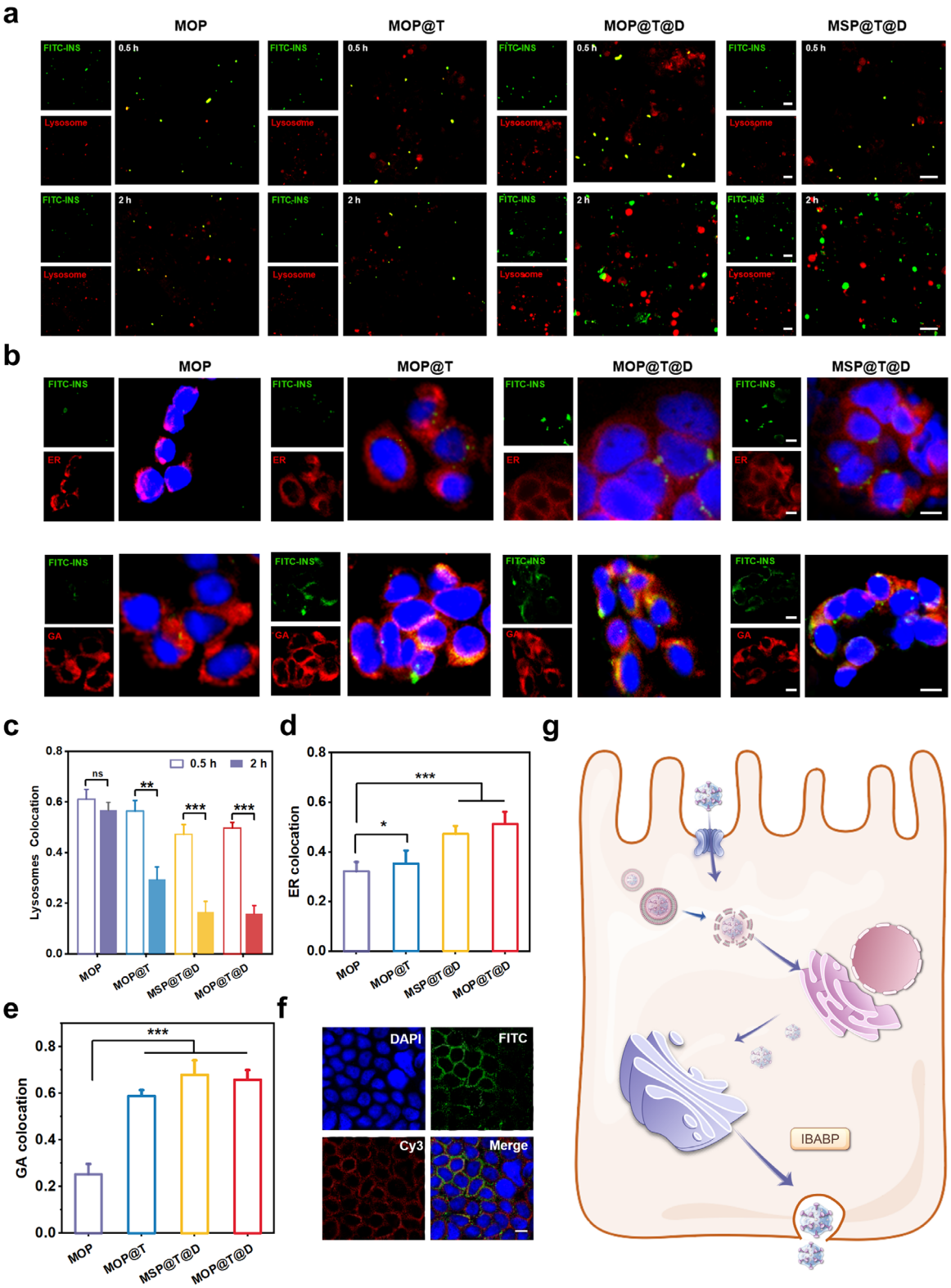

Figure 4. Studies on intracellular transport and exocytosis of MOP@T@D. a) Colocalization analysis of FITC-INS-loaded nanoparticles (green) with lysosomes (red) at 0.5 and 2 h ($n = 3$). Scale bar: 10 μm. b) Colocalization analysis of nanoparticles (green) and ER/Golgi (red) by CLSM ($n = 3$). Scale bar: 10 μm. The colocalization coefficient of nanoparticles with c) lysosomes, d) ER, and e) Golgi ($n = 3$). f) CLSM visualization of the interaction between FITC-insulin-loaded MOP@T@D (green) and intestinal bile acid-binding protein IBABP ($n = 3$). Scale bar: 10 μm. g) Schematic illustration of the intracellular transcytosis pathway of MOP@T@D. Data presented as means ± SD. Statistical analysis was performed using one-way ANOVA with Tukey's multiple comparisons test. $^*P < 0.05$; $^{**}P < 0.01$; $^{***}P < 0.001$; ns, no significant difference.

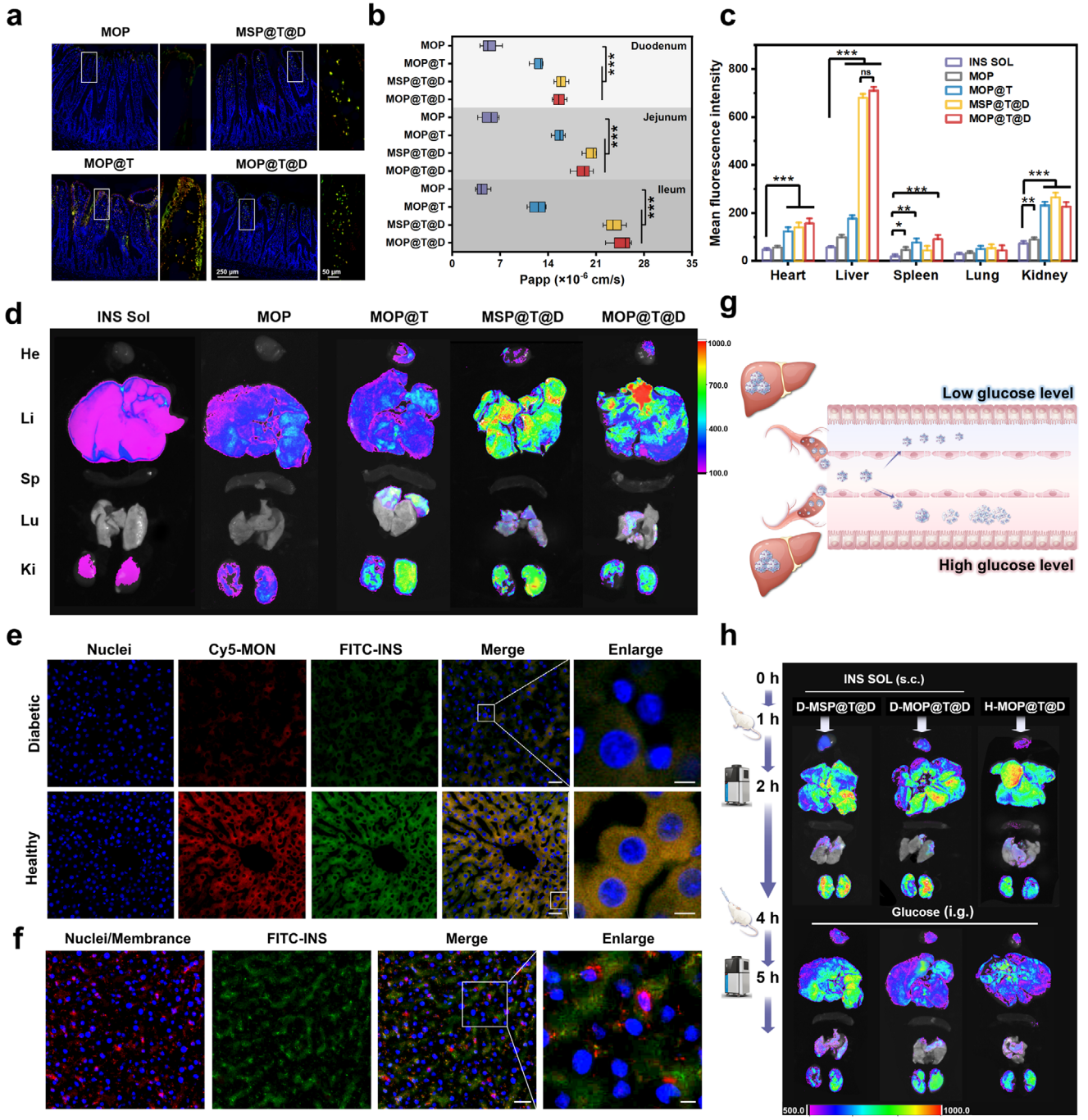

Figure 5. MOP@T@D improved intestinal permeability and achieved efficient liver accumulation to mimicking the action of endogenous insulin. a) Ileum sections images after incubated with dual-fluorescent-labeled MOP@T@D (FITC-INS and Cy5-MON) ($n = 3$). Scale bars: 250 and 50 μm (magnified inset). b) Papp values of nanoparticles in different intestinal segments ($n = 5$). c) Semi-quantitative analysis of biodistribution of nanoparticles in major organs of healthy SD rats ($n = 3$). d) Tissue distribution of FITC-INS-loaded nanoparticles after oral administration by IVIS. He, heart; Li, liver; Sp, spleen; Lu, lung; Ki, kidney ($n = 3$). e) Hepatic accumulation of MOP@T@D in healthy and diabetic rats following oral administration ($n = 3$). Scale bars: 50 and 10 μm (magnified inset). Nuclei: Hoechst 33 342 (blue). f) Precise localization of MOP@T@D in the liver. Nuclei: Hoechst 33 34 2 (blue); cytomembrane: Alexa 555-WGA (red) ($n = 3$). Scale bars: 50 and 10 μm (magnified inset). g) Schematic diagram of responsive release of MOP@T@D within Disse space. h) Biodistribution of FITC-INS loaded MSP@T@D and MOP@T@D in healthy (abbreviated as H) and diabetic (abbreviated as D) rats before and after a glucose challenge, demonstrating glucose-responsive dissociation of MOP@T@D ($n = 3$). Data presented as means ± SD. Statistical analysis was performed using one-way ANOVA with Tukey's multiple comparisons test. $^*P < 0.05$; $^{**}P < 0.01$; $^{***}P < 0.001$; ns, no significant difference.

contrast, diabetic rats showed markedly reduced fluorescence, suggesting glucose-triggered disassembly of MOP@T@D under hyperglycemic conditions. MOP@T@D was precisely located in the perisinusoidal space (Disse space), a strategic location adjacent to hepatocytes (Figure 5f). This strategic localization enabled released insulin to directly bind insulin receptors on hepatocytes, activating downstream signaling to promote hepatic glucose uptake and glycogen synthesis (Figure 5g). The hepatic retention of MOP@T@D mirrored the natural enterohepatic circulation of bile acids, leveraging endogenous pathways for site-specific enrichment.

To quantitatively assess the glucose-responsive behavior of MOP@T@D, the dynamic fluorescence tracking of nanoparticles was performed in healthy and diabetic rats. To temporarily normalize blood glucose levels, diabetic rats received a subcutaneous insulin injection at time zero. All rats received the designated oral formulations at 1 h and an oral glucose challenge to induce hyperglycemia at 4 h. The hepatic fluorescence intensity (FI) ratio (5 h/2 h) was calculated, which was negatively correlated with the degradation of nanoparticles. Diabetic rats treated with MOP@T@D showed a 43.7% FI retention ratio, significantly lower than the 57.6% observed in healthy rats (Figure 5h; Figure S24, Supporting Information), suggesting that MOP@T@D compensated for impaired glucose regulation in diabetic rats. Moreover, the fluorescence retention of MOP@T@D was 40% lower than that of the non-responsive MSP@T@D in diabetic rats, further confirming its glucose-dependent release profile. By combining Disse space targeting with glucose responsiveness, MOP@T@D successfully mimicked the biphasic insulin secretion pattern of β-cells, remaining stable during normoglycemia while rapidly releasing insulin in response to hyperglycemia.

2.6. MOP@T@D Enhanced Oral Insulin Bioavailability and Restored Glucose Homeostasis

Achieving sustained glucose homeostasis without hypoglycemic risk remains a critical unmet need in diabetes therapy. Hypoglycemic effect and pharmacokinetics of various formulations were evaluated in diabetic rats. Pharmacokinetic profiling demonstrated that oral MOP@T@D sustainably released insulin for 12 h, with a bioavailability of 6.8%, which was 1.6-fold and 1.8-fold higher than MOP@T (4.3%) and MSP@T@D (3.7%) (**Figure 6a**). In contrast, subcutaneous insulin showed rapid systemic clearance and only transient glycemic control. The blood glucose–time curve further highlighted the challenges of oral insulin solution delivery, owning to rapid degradation and absorption barriers in the gastrointestinal tract (Figure 6b).[30] Notably, MOP@T@D induced a maximum glucose reduction of 33.5% in diabetic rats, with a pharmacological bioavailability of 10.6%, while MSP@T@D was only 5%. These results underscored the advantages of MOP@T@D in intestinal penetration, hepatic accumulation, and glucose-responsive release.

In the oral glucose tolerance test, MOP@T@D rapidly restored normoglycemia (Figure 6c), closely mimicking physiological insulin secretion. A transient rise in serum insulin levels further confirmed its glucose-triggered release behavior (Figure 6d). Importantly, compared with insulin solution, MOP@T@D treatment resulted in more stable blood glucose levels (Figure 6e) and reduced the hypoglycemic index by 67% (Figure 6f). This avoided the common hypoglycemic risk in current insulin therapy and greatly enhanced the safety of medication.

The effects of long-term MOP@T@D administration on glucose metabolism were examined in healthy and diabetic rats (Figure 6g). Promoting glycogen production is key for insulin to regulate glucose homeostasis, helping to lower blood glucose levels and buffer glucose fluctuations. Diabetic rats (DC) groups exhibited a 3.2-fold depletion in hepatic glycogen compared to healthy controls (NC) (Figure 6h), which is consistent with the characteristics of impaired glucose metabolism. In contrast, MOP@T@D restored glycogen reserved to 2.6-fold of DC groups, outperforming both subcutaneous insulin (1.5-fold) and MSP@T@D (1.4-fold) (Figure 6i).

Mechanistically, MOP@T@D functioned as a glucose-responsive insulin reservoir within the hepatic sinusoids. The released insulin activated the hepatic insulin receptor, upregulating IRS-1, enhancing AKT phosphorylation, and suppressing GSK3-β activity (Figure 6j,k), thereby promoting glycogen synthesis and inhibiting gluconeogenesis. Crucially, hepatic glycogen serves as the primary glucose reservoir that can be directly mobilized to maintain systemic glucose homeostasis, unlike muscle glycogen which functions solely as a local energy source.[31] Compared to subcutaneous injection—which causes peripheral hyperinsulinemia and insufficient hepatic insulin signaling—oral MOP@T@D enables hepatic uptake through the portal vein, directly activating the hepatic IRS-1/AKT/GSK3-β axis (Figure 6l). This liver-targeted approach enhanced glycogen synthesis and suppressed gluconeogenesis, resulting in more physiological glucose control with reduced hypoglycemia risk.[32]

2.7. Substantial Benefit of MOP@T@D for β-Cell Protection

2.7.1. β-Cell Protection through Selenoproteins-Driven Antioxidant Activation

Chronic hyperglycemia fuels a self-perpetuating cycle of oxidative stress and inflammation, leading to β-cell dysfunction in T2DM.[33] MOP@T@D disrupted this vicious cycle by leveraging selenium's dual role as a glucose-responsive release trigger and a metabolic precursor for antioxidant defense. Diabetic rats treated with MOP@T@D exhibited a 3.6-fold increase in selenocysteine ($SeCys_2$) compared to MSP@T@D by HPLC-ICP-MS analysis (**Figure 7a**).[34] Any protein that incorporates $SeCys_2$ into a polypeptide chain is defined as a selenoprotein, some of which have been identified as antioxidant enzymes to inhibit oxidative stress-induced damage, such as glutathione peroxidase (Gpx), thioredoxin reductase (TrxR), and selenoprotein K (SelK).[35] Compared with the DC group, MOP@T@D enhanced Gpx activity by 31% and elevated superoxide dismutase (SOD) levels by 18%, while suppressing lipid peroxide (MDA) by 30% ($P < 0.001$ for Gpx; $P < 0.05$ for SOD and MDA; Figure 7b–d). qPCR analysis also confirmed upregulation of selenoprotein genes (Gpx1, Gpx4, TrxR1, TrxR2, and SelK) (Figure 7e), establishing a systemic antioxidant shield that mitigates β-cell oxidative damage.

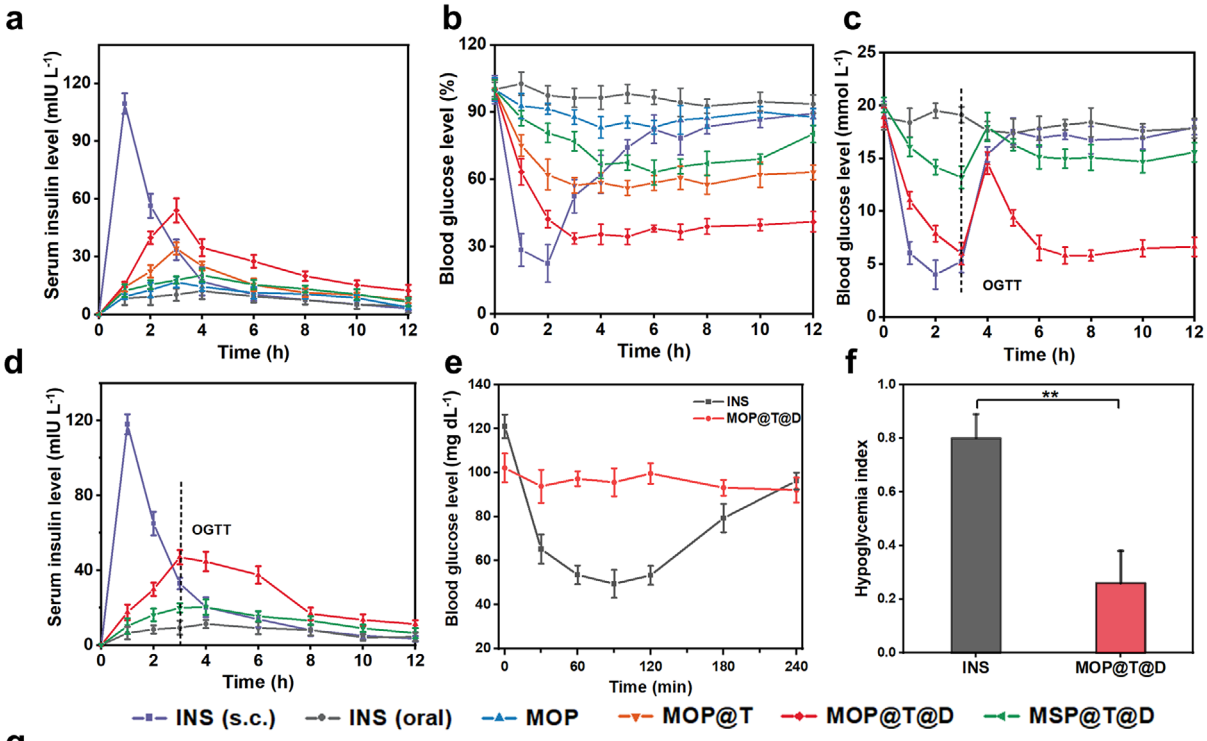

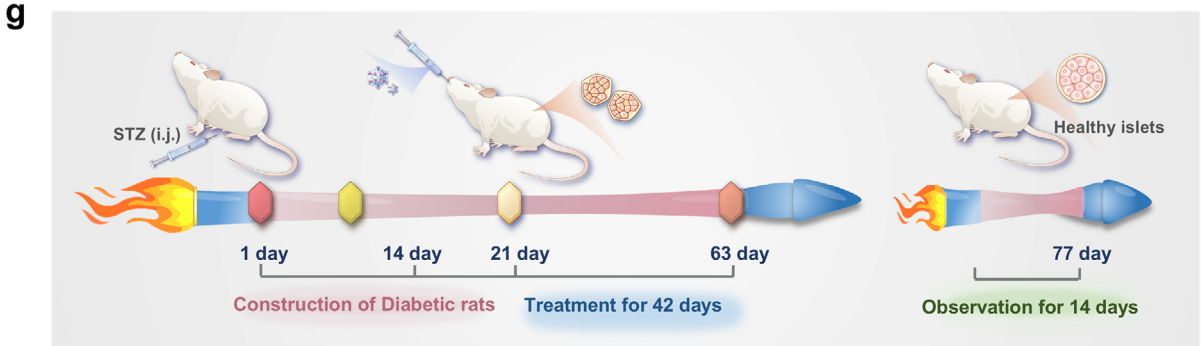

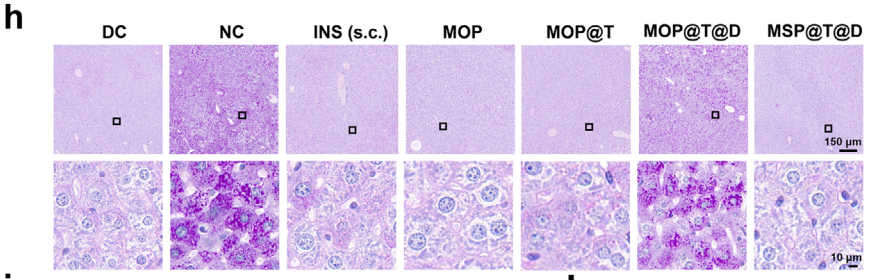

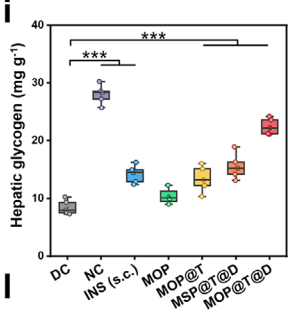

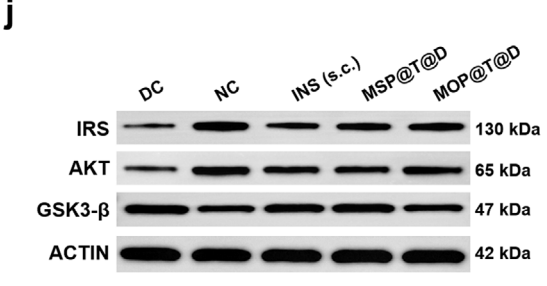

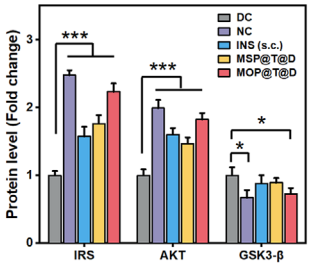

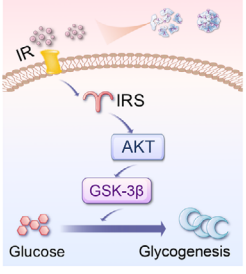

A distinctive characteristic of the diselenide-bridged mesoporous organosilica nanoparticles in MOP@T@D was their responsive biodegradation behavior.[36] Under hyperglycemic conditions, the cleavage of the diselenide bond led to the disintegration of MON. The resulting selenium-containing metabolites are subsequently processed in hepatocytes to generate $SeCys_2$ and, ultimately, functional selenoproteins, thereby boosting cellular antioxidant defenses.[37] However, the detailed kinetics of MON degradation and selenoproteins maturation remain partially understood and warrant further investigation using real-time tracking strategies in physiologically relevant settings.[38]

2.7.2. NF-κB Inactivation Reversed Inflammation-Driven β-Cell Dysfunction

Beyond redox regulation, the selenium derivatives mitigated hyperglycemia-induced inflammatory cascades.[39] In diabetic islets, the NF-κB pathway—a central regulator of pro-inflammatory signaling—was markedly activated (Figure 7f), as indicated by elevated p-p65/p65 (1.6-fold) and p-IκB-α/IκB-α (1.8-fold) ratios compared to the NC group (Figure 7g). Treatment with MOP@T@D significantly suppressed these phosphorylation events by 31% and 22%, respectively, effectively inhibiting NF-κB nuclear translocation. This inhibition translated to a 49% reduction in IL-1β (Figure 7h), 53% reduction in TNF-α (Figure 7i), and 59% reduction in IL-6 ($P < 0.001$ vs DC group, Figure 7j), thereby attenuating the inflammatory microenvironment. Selenoproteins generated from MOP@T@D neutralized ROS, thereby disrupting the ROS–NF-κB feedforward amplification loop (Figure 7k). This coordinated action contributed to the recovery of insulin secretion capacity in diabetic rats, breaking the self-perpetuating cycle of glucotoxicity and β-cell dysfunction.

2.8. Positive Intervention of MOP@T@D for Diabetes

2.8.1. Pancreatic β-Cell Regeneration and Functional Recovery

MOP@T@D could break the vicious cycle of hyperglycemia, oxidative stress, and inflammation in diabetes, potentially leading to positive interventions for diabetes and its complications. Long-term treatment with MOP@T@D led to significant restoration of pancreatic islet morphology and function, as evidenced by immunofluorescence staining for insulin and glucagon (**Figure 8a**). Specifically, insulin levels in the MOP@T@D group were 4.9-fold and 2.3-fold higher than those in the DC group and MSP@T@D group, respectively (Figure S25a,b, Supporting Information). Histological examination using H&E staining revealed significant degenerative changes and marked atrophy of the islets in the DC group (Figure 8b). In contrast, the MOP@T@D group exhibited well-defined islet boundaries, a denser distribution of β-cells, and a 26.7% increase in islet area compared to the DC group (Figure 8c). Moreover, pancreatic insulin secretion in the MOP@T@D group returned to 74.6% of the physiological level (Figure 8d). These findings collectively indicated that MOP@T@D not only reversed the loss of β-cells but also promoted their regeneration and enhances secretory function in type 2 diabetic rats. The protective effect of the metabolite $SeCys_2$ of MOP@T@D on INS-1 cells was investigated. The insulin secretion level of INS-1 cells was increased by 47% compared to the palmitic acid-exposed controls (Figure 8e).

Critically, the therapeutic benefits of MOP@T@D were sustained beyond the treatment period. Two weeks after dosing cessation, MOP@T@D-treated rats maintained normoglycemia, whereas the MSP@T@D group reverted to hyperglycemia (Figure 8g). This sustained glucose stability indicated that MOP@T@D promoted functional β-cell regeneration rather than merely providing a transient insulin supplement. In contrast, although MSP@T@D improved insulin delivery to the liver, it failed to restore β-cell mass or glucose control.

2.8.2. Restoration of Systemic Metabolic Homeostasis

Beyond its restorative effects on pancreatic β-cells, MOP@T@D improved diabetes-associated systemic metabolic dysfunction. Treatment with MOP@T@D significantly improved the serum lipid profile, a major contributor to β-cell lipotoxicity, by reducing triglyceride (TG) by 43% (Figure 8f), total cholesterol (TC) by 39% (Figure 8h), and low-density lipoprotein (LDL) by 35% (Figure 8i), while increasing high-density lipoprotein (HDL) by 30% (Figure 8j). Additionally, glycated hemoglobin (HbA1c), a key indicator of chronic hyperglycemia, was reduced by 30% (Figure 8k).[40] The rats body weights of the MOP@T@D group were also well controlled (Figure S26, Supporting Information), further supporting its systemic metabolic benefits.

Therapeutic efficacy was further evidenced by insulin resistance reversal. MOP@T@D significantly lowered HOMA-IR values versus the DC group ($P < 0.001$), confirming restored hepatic insulin sensitivity (Figure 8l). Concurrently, HOMA-β indices reached 82% of normal levels, confirming substantial restoration of functional β-cell mass (Figure 8m). These comprehensive improvements stemmed from dual synergistic mechanisms. First, glucose-responsive insulin release within hepatic tissue rapidly mitigated glucotoxicity, reactivating IRS-1/AKT signaling to restore systemic insulin sensitivity. Second, antioxidant

Figure 6. MOP@T@D enhanced oral insulin bioavailability and restored glucose homeostasis. a) Serum insulin and b) blood glucose level of diabetic rats after administration of insulin solution (s.c., 5 IU kg^{-1}) or oral formulations of insulin solution, MOP, MOP@T, MSP@T@D, and MOP@T@D (80 IU kg^{-1}) ($n = 3$). c) Blood glucose and d) serum insulin level after administration of insulin solution (s.c., 5 IU kg^{-1}) or oral formulations of insulin solution, MSP@T@D, and MOP@T@D (80 IU kg^{-1}), followed by a glucose challenge (2 g kg^{-1}) at 3 h ($n = 5$). e) Blood glucose levels in healthy rats after subcutaneous injection of insulin and MOP@T@D ($n = 5$). f) Quantification of the hypoglycemic index ($n = 5$). g) Schematic representation of the experimental protocol for diabetic rats. h) Liver glycogen staining and i) quantitative analysis after treatment ($n = 5$). Scale bars: 150 and 10 μm (magnified inset). DC: diabetic control group; NC: normal control group. j) Western blot analysis and k) semi-quantification of IRS-1, AKT, and GSK3-β expression in liver tissue ($n = 5$). l) Schematic representation of signaling for hepatic glycogen synthesis in hepatocytes after insulin stimulation. Data presented as means ± SD. Statistical analysis was performed using one-way ANOVA with Tukey's multiple comparisons test. *$P < 0.05$; **$P < 0.01$; ***$P < 0.001$; ns, no significant difference.

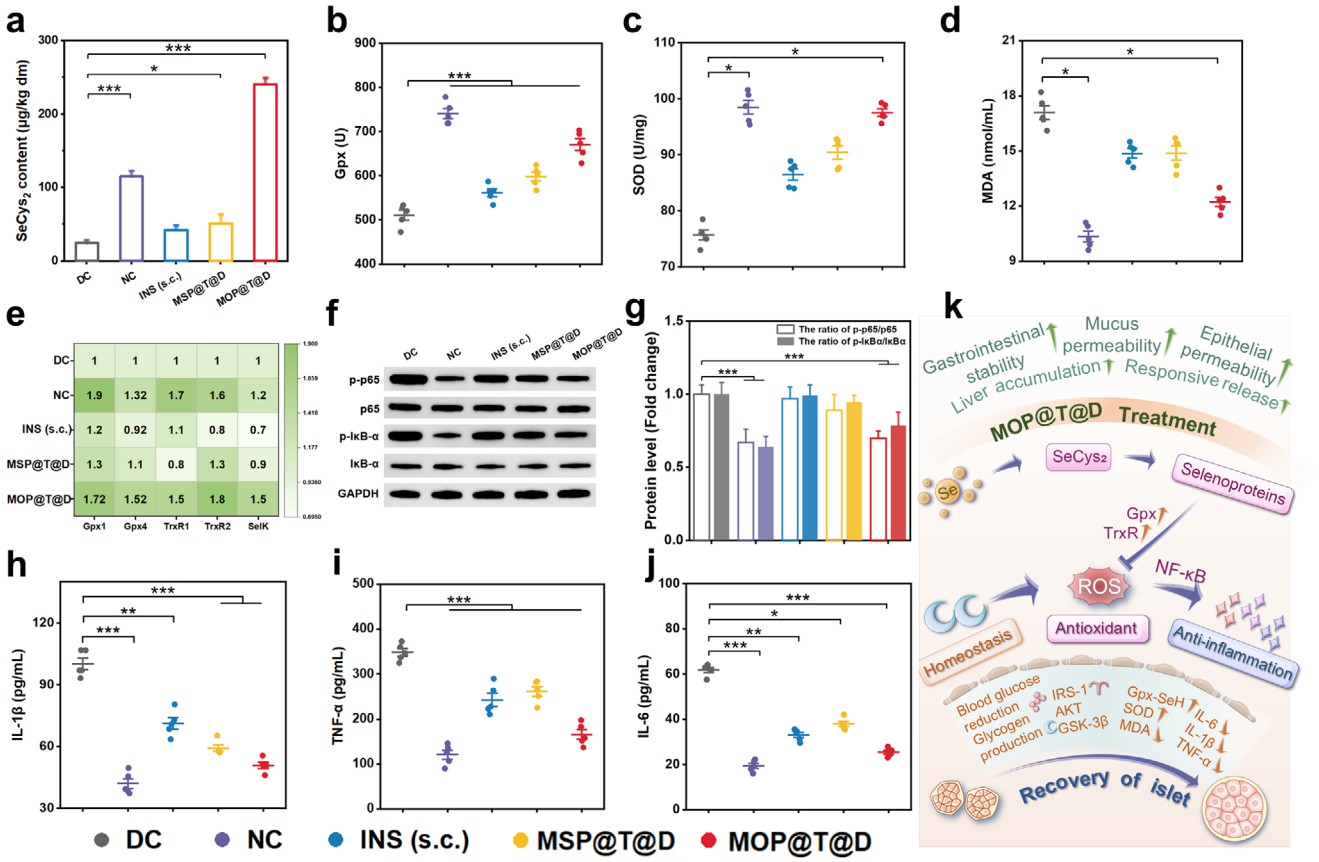

Figure 7. MOP@T@D protected pancreatic β-cells via antioxidant and anti-inflammatory pathways. a) Quantitative analysis of $SeCys_2$ in islet by HPLC-ICP-MS ($n = 5$). Antioxidant enzyme activities and oxidative stress markers in diabetic rats after 6 weeks of treatment: b) glutathione peroxidase (GPx) activity, c) superoxide dismutase (SOD) level, and d) malondialdehyde (MDA) content ($n = 5$). e) Relative mRNA expression levels of selenoprotein genes (Gpx1, Gpx4, TrxR1, TrxR2, and SelK) measured by qPCR ($n = 5$). f) Western blot analysis and g) quantitative analysis of p-p65/p65 and p-IκB-α/IκB-α ratios in islet tissues ($n = 5$). Inflammatory factor levels of h) IL-1β, i) TNF-α, and j) IL-6 in different treatment groups ($n = 5$). k) Schematic diagram illustrating the proposed mechanism by which MOP@T@D alleviated oxidative stress and inflammation in diabetic β-cells. Data presented as means ± SD. Statistical analysis was performed using one-way ANOVA with Tukey's multiple comparisons test. *$P < 0.05$; **$P < 0.01$; ***$P < 0.001$; ns, no significant difference.

metabolites from MOP@T@D degradation eliminated islet ROS, blocking ROS-NF-κB cascades to reverse inflammation-driven insulin resistance while promoting β-cell regeneration.

2.9. In Vivo Biocompatibility of MOP@T@D

The safety profile of MOP@T@D was evaluated in healthy SD rats administered for six weeks. Selenium levels in liver, kidney, heart, spleen, and lung tissues before and after MOP@T@D administration were quantified by ICP-MS. The results revealed predominant selenium accumulation in the liver. Notably, hepatic selenium levels returned to normal within 5 days post-treatment cessation (**Figure 9a**). This rapid clearance was consistent with elevated levels of selenocysteine and glutathione peroxidase, suggesting active selenium metabolism. Critically, serum immunoglobulin G (IgG, Figure 9b) and immunoglobulin M (IgM, Figure 9c) levels in rats demonstrated no significant immunogenicity for MOP@T@D. This finding further indicated the immunologically safety of MOP@T@D and its degradation products.

There was no significant difference in liver alanine aminotransferase (ALT) (Figure 9d), aspartate aminotransferase (AST) (Figure 9e), and serum creatinine (CREA) (Figure 9f) between the control group and the experimental group, which proved the liver and kidney safety of MOP@T@D. Histopathological analysis confirmed biocompatibility, with no observable intestinal or organ toxicity relative to the control group (Figure 9g). In addition, we conducted cytotoxicity evaluation using the non-cancerous mouse hepatocyte line AML12 under high glucose conditions (25 mM). The results demonstrated that cell viability in the MOP@T@D treatment group showed no significant difference compared to the high glucose control group (Figure S27, Supporting Information), providing important evidence for the safety of MOP@T@D at the cellular level. These integrated findings demonstrated favorable in vivo biocompatibility and underscored the therapeutic potential of MOP@T@D for long-term diabetes management.

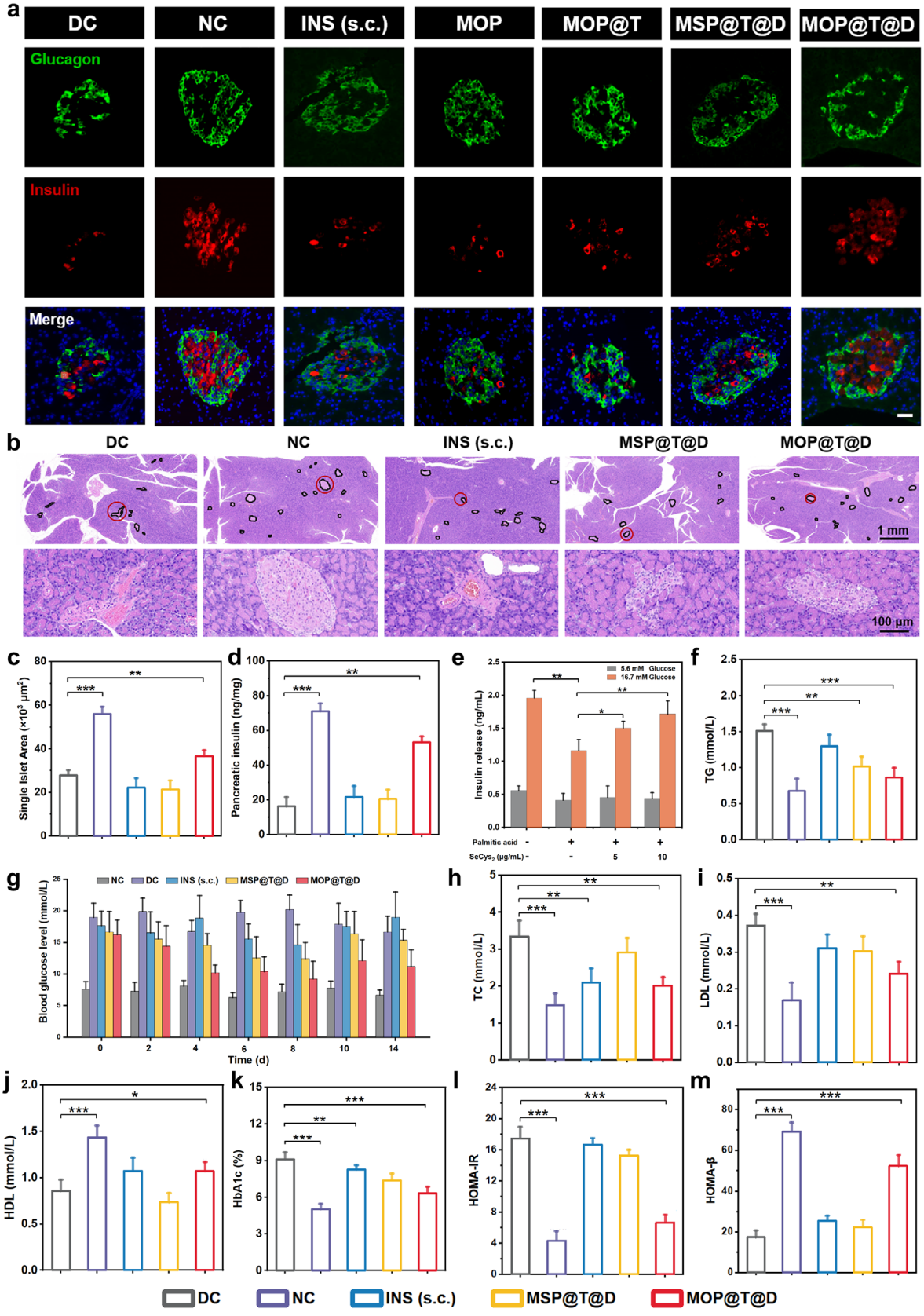

3. Conclusion

In this study, we developed an oral nano-therapeutic platform, MOP@T@D, which combined glucose-responsive insulin release with selenium-based antioxidant protection to address the core pathological issues of T2DM. This system used mesoporous organosilicon nanoparticles functionalized with deoxycholic acid to achieve efficient intestinal absorption and hepatotropic targeting, achieving a remarkable oral bioavailability of 10.6%. The platform effectively upregulated key antioxidant selenoproteins, mitigating oxidative stress and suppressing inflammatory responses. This nanosystem represented a functional evolution from a mere drug carrier to an active therapeutic agent, offering an innovative strategy for long-term T2DM management.

Future investigations will focus on establishing comprehensive safety profiles through chronic toxicity assessments in large animal models, with particular attention to selenium biodistribution and tissue accumulation patterns. The pharmacokinetic behavior also needs to be further investigated, including speciation analysis to track selenium metabolites and correlation of carrier degradation kinetics with drug release profiles. In addition, particular attention should be paid to batch-to-batch consistency in drug loading and selenium content, as well as the precise control of surface ligand density for successful scale-up production.

This organosilica platform offers substantial potential for expansion beyond insulin delivery. Strategic modification of organic bridging units enables precise tuning of degradation rates and release kinetics, allowing customization for diverse therapeutic requirements. The versatile surface functionalization supports adaptation to various biologic therapeutics, including GLP-1 analogs and nucleic acid-based drugs, creating opportunities for combination therapies in metabolic diseases. Furthermore, the intrinsic antioxidant properties of the platform suggest promising utility in managing other oxidative stress-related pathologies, such as neurodegenerative disorders and cardiovascular diseases. In summary, this work establishes organosilica nanoparticles as a transformative platform that transcends traditional drug delivery concepts through integrated therapeutic functionality. By addressing both symptomatic management and underlying pathophysiology, this technology provides a foundation for next-generation nanotherapeutics with enhanced clinical relevance and translation potential.

4. Experimental Section

Materials: Caco-2 and HT29-MTX-E12, were provided by EK-Bioscience (Shanghai, China). Porcine insulin was purchased from Wanbang Biochemical Pharmaceutical Co., Ltd., China. Selenium (Se) powder, sodium borohydride ($NaBH_4$), ammonium nitrate (NH_4NO_3), and hydrogen peroxide (30% H_2O_2) were purchased from Beijing Chemical Reagent Co. (Beijing China). Tetraethyl orthosilicate (TEOS), γ-chloropropyl trimethoxysilane (CP), 3-etyltrimethylammonium tosylate (CTAT), 1,6-Bis (Triethoxysilyl) Hexane (BTESiH), aminopropyltriethoxysilane (APTES), triethanolamine ($TEAH_3$), FITC, RITC, streptozotocin (STZ), carbodiimide hydrochloride (EDC), and N-hydroxy succunimide (NHS) were purchased from Shanghai Aladdin Bio-Chem Technology Co., Ltd, China. Sodium deoxycholate (Dc) was purchased from Beijing Voke Biotechnology Co., Ltd, China. Transferrin was purchased from Beyotime Biotechnology Co., Ltd, China. GOx, DAPI, Cy5-NHS, DMEM, FBS, and 0.25% trypsin-EDTA were purchased from Dalian Meilum Co., Ltd.

Synthesis and Characterization of BTESePD: The diselenide-bridged organosilica precursor, bis[3-(triethoxysilyl)propyl] diselenide (BTESePD), was synthesized by reacting γ-chloropropyltrimethoxysilane with freshly prepared sodium diselenide, following a previously reported procedure.[41] Detailed synthetic procedures are provided in the Supporting Information. The chemical structure of BTESePD was verified by ^{1}H NMR, ^{13}C NMR, and mass spectrometry.

Preparation of MOP@T@D and MSP@T@D: MON were prepared by the sol–gel method, in which the co-silicon sources were ethyl orthosilicate (TEOS) and BTESePD.[42] Detailed methods are described in the Supporting Information. For the preparation of MOP, 1 mL of insulin solution (10 mg mL^{-1}) and 1 mL of GOx solution (2 mg mL^{-1} in ddH_2O) were added dropwise to 10 mL of MON dispersion (0.5 mg mL^{-1} in PBS, pH 7.4) stirring for 12 h at room temperature to obtain MOP. MOP were collected by centrifugation and washed three times with ddH_2O to remove free INS and GOx that attached to the external surface of the MON. Subsequently, 1 mL of Tf solution (5 mg mL^{-1}, containing EDC 2.5 mg mL^{-1}, NHS 2.5 mg mL^{-1}) was dripped into the MOP dispersion. The reaction proceeded under stirring for 24 h at room temperature to form amide bonds between carboxyl groups of Tf and surface amine groups on MOP, yielding MOP@T. Finally, 500 µL of deoxycholic acid solution (5 mg mL^{-1}, containing of EDC 2.5 mg mL^{-1}, NHS 2.5 mg mL^{-1}) was added to the MOP@T dispersion and stirred for another 24 h to obtain the final product, MOP@T@D. The control nanoparticles, MSP@T@D, were prepared following an identical procedure. For comparative purposes, non-responsive MSN were prepared similarly using 1,6-Bis (Triethoxysilyl) Hexane (BTESiH) instead of BTESePD under identical conditions.

The unloaded insulin and GOx concentrations in the supernatant of the crude MOP were quantified using an HPLC method (Agilent 1260) and a Glucose Oxidase Activity Assay Kit (Elabscience, China), respectively. The loading content of insulin and GOx was calculated by Equation (1).

$$\text{Loading content} = W_{sup}/W_{NPs} \times 100\% \quad (1)$$

where W_{sup} is the weight of unloaded insulin or GOx in supernatant, W_{NPs} is the weight of MOP@T@D.

Synthesis Validation and Characterization: The size and zeta potential of nanoparticles were measured by Malvern Zetasizer Nano ZS-90. The morphology of nanoparticles was observed via TEM (Hitachi H-600). FTIR spectra were measured using a Bruker VECTOR-22 spectrometer. XPS spectra were collected by Thermo Fisher Scientific Nexsa G2. Fluorescence intensity of dual-labeled formulation (FITC-Insulin and RITC-Tf) was measured using a Molecular Devices SpectraMax M3 microplate reader (excitation: 425 nm; emission: 485–700 nm). BET was used to investigate the structural properties of mesoporous materials. Elemental mapping analysis was performed by FEI Talos F200X G2. The synthesis method of FITC-Insulin is as shown in the Supporting Information.

In Vitro Glucose-Responsive Release Study: To confirm the sensitivity to H_2O_2, the size changes of MON@T@D and release profiles of

Figure 8. MOP@T@D protected pancreatic β-cell function and mass in diabetic rats. a) Representative immunofluorescence images of pancreatic islets from diabetic rats after 6 weeks of treatment ($n = 5$). Scale bar: 50 µm. b) H&E staining and c) quantitative analysis of islet area ($n = 5$). Black circles indicate islets. Scale bars: 1 mm and 100 µm (magnified inset). d) Pancreatic insulin content across treatment groups ($n = 5$). e) Effects of $SeCys_2$, a metabolite of MOP@T@D, on insulin secretion in INS-1 cells under low (5.6 mM) and high glucose (16.7 mM) conditions, respectively ($n = 5$). f) Serum TG levels of rats after treatment for six weeks ($n = 5$). g) Blood glucose level of rats during treatment and after stopping administration for another two weeks ($n = 5$). Serum level of h) TC, (i) LDL, and j) HDL of rats after treatment for six weeks ($n = 5$). Metabolic parameters including k) HbA1c, l) HOMA-IR, and m) HOMA-β ($n = 5$). Data presented as means ± SD. Statistical analysis was performed using one-way ANOVA with Tukey's multiple comparisons test. *$P < 0.05$; **$P < 0.01$; ***$P < 0.001$; ns, no significant difference.

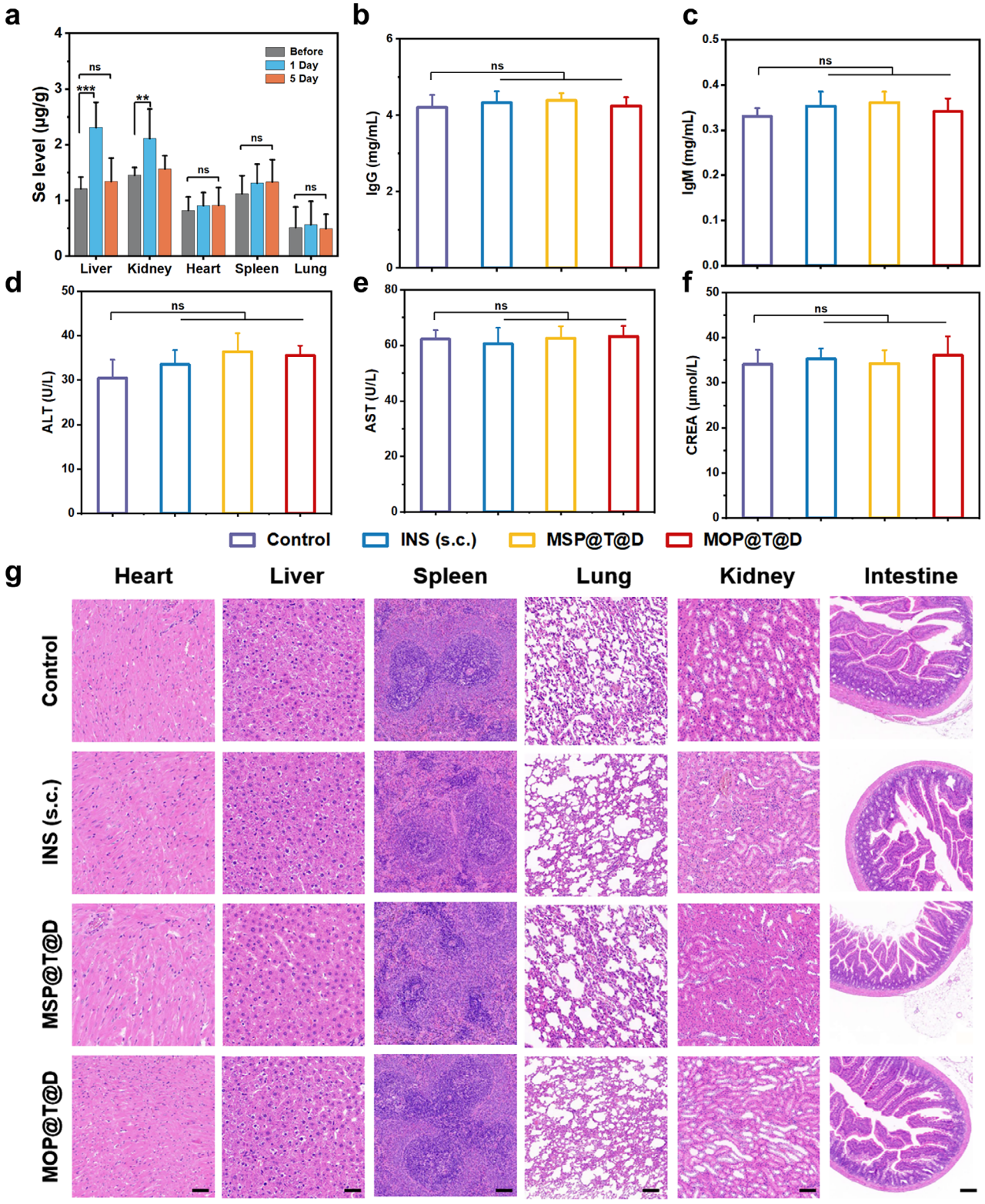

Figure 9. In vivo biocompatibility of MOP@T@D. a) Se concentration in liver, kidney, heart, spleen, and lung tissues measured by ICP-MS before and after six weeks of MOP@T@D treatment ($n = 5$). Serum levels of b) Ig G and c) Ig M in healthy rats after treating with different formulations ($n = 5$). Serum levels of d) ALT, e) AST, and f) CREA in healthy rats after treating with different formulations ($n = 5$). g) H&E staining results of the main organ sections of healthy rats after treatment for six weeks ($n = 5$). Scale bar: 100 μm. Data presented as means ± SD. Statistical analysis was performed using one-way ANOVA with Tukey's multiple comparisons test. *$P < 0.05$; **$P < 0.01$; ***$P < 0.001$; ns, no significant difference.

MOP@T@D were studied by incubation with different concentrations of H_2O_2. The size changes were determined, and the FRET emission of the dual-labeled formulation (FITC-MON and RITC-Tf) was measured using an enzyme marker under 425 nm excitation. At predetermined time points, samples were extracted for TEM observation at 24 and 72 h after incubation, respectively.

To mimic oral administration, MOP@T@D was incubated in SGF (2 h) and then in SIF (6 h). Glucose-responsive insulin release was evaluated by incubating MOP@T@D (10 mg) in PBS containing varying glucose levels (0, 100, 200, 300, and 400 mg dL^{-1}) at 37 °C with shaking. At predetermined time points, 50 µL aliquots samples were collected, centrifuged (10 000 g, 10 min), and analyzed by HPLC. Besides, insulin release from MOP@T@D in repeated cycles of high, medium, and low glucose concentrations was investigated. Briefly, MOP@T@D (10 mg) was serially incubated and transferred in glucose-containing PBS (1 mL) at 400 mg dL^{-1} (for 1 h), 200 mg dL^{-1} (for 1 h), and 100 mg dL^{-1} (for 4 h) at 37 °C, respectively. A pulse release profile was also studied by alternating between 400 and 100 mg dL^{-1} glucose solutions. Insulin concentration was determined by HPLC. The structural changes of MSP@T@D and MOP@T@D were observed by TEM. The HPLC method for insulin is detailed in the Supporting Information.[43]

In Vitro Stability Study: The secondary structure and pharmacological activity of the released insulin were examined. In addition, the stability of MOP@T@D in simulated gastric fluid (SGF), simulated intestinal fluid (SIF), as well as 3 mM bile salts was investigated. Detailed methods are described in the Supporting Information.

Cell Culture: Caco-2 and HT29-MTX-E12 cells were provided by EK-Bioscience (Shanghai, China). Caco-2 cells were cultured in DMEM medium with 20% (v/v) FBS, 1% penicillin, and streptomycin (100 IU mL^{-1}) at 37 °C in 5% CO_2. HT29-MTX-E12 cells were cultured in DMEM medium with 10% (v/v) FBS, 1% (v/v) nonessential amino acids, 1% penicillin, and streptomycin (100 IU mL^{-1}) at 37 °C in 5% CO_2. INS-1 cells were provided by Meisen CTCC (Shanghai). INS-1 cells were cultured in RPMI medium supplemented with 10% FBS, 1 mM glutamine, 50 µM β-mercaptoethanol, 1% penicillin, and streptomycin (100 IU mL^{-1}) at 37 °C in 5% CO_2.

Mucus Permeability Study: Multiple particle tracking and 3D mucus model tests were performed using previously described methods,[44] as detailed in the Supporting Information. To evaluate the mucus permeability of nanoparticles in a Transwell system (Corning, pore size: 0.4 µm), 80 µL of porcine mucus was placed into the donor chamber and 800 µL of PBS (pH 7.4) into the acceptor chamber. After 30 min of equilibration on a shaker at 37 °C, FITC-INS-loaded MSP, MOP, MSP@T, MOP@T, MSP@T@D, or MOP@T@D (FITC-INS concentration: 50 µg mL^{-1}) was added to the donor chamber. Aliquots of 100 µL were collected from the acceptor chamber at designated time points and analyzed using a microplate reader to calculate the apparent permeability coefficient (Papp).

To assess the mucus penetration ability of nanoparticles, HT29-MTX-E12 cells were seeded at a density of 5×10^4 cells per well in Transwell inserts (Corning, pore size: 0.4 µm). The cell monolayers were incubated with either FITC-INS solution or FITC-INS-loaded nanoparticles at an FITC-INS concentration of 50 µg mL^{-1} for 2 h at 37 °C. Cells were then washed three times with PBS, followed by staining of mucus with Alexa Fluor 488-conjugated WGA for 30 min and three additional PBS washes. Fluorescence was imaged in three dimensions using a CLSM.

Cytotoxicity Study: CCK-8 assay was used to detect the viability of Caco-2 and HT29-MTX-E12 cells at different nanoparticle concentrations (0–1000 µg mL^{-1}). Detailed methods are described in the Supporting Information.

Transepithelial Transport Study: For the co-culture of Caco-2 and HT29-MTX-E12 cells, a physiologically representative ratio of 9:1 (Caco-2:HT29-MTX-E12) was used for cell seeding. Cells were seeded on Transwell inserts (0.4 µm pore size; Corning) at a density of 5×10^4 cells per well and maintained for 21 days to form mature monolayers. TEER was assessed continuously throughout the 21-day differentiation period (Milli cell-ERS, Millipore). Monolayers demonstrating TEER values of at least 1000 $\Omega \times cm^2$ were considered fully functional and suitable for subsequent experiments.

After equilibration in HBSS for 30 min at 37 °C, FITC-Insulin labeled nanoparticles (FITC-INS concentration: 50 µg mL^{-1}) were added to assess in vitro permeability. At predetermined time intervals, 200 µL of basolateral medium was sampled and replaced with an equal volume of fresh PBS. TEER was measured at each time point, and Papp was calculated accordingly. To further investigate whether MOP@T@D could open tight junctions, immunofluorescence staining for occludin was performed. Fixed cells were incubated with a primary antibody against occludin for 30 min at room temperature, followed by a secondary antibody (anti-rabbit IgG Fab2 conjugated to Alexa Fluor 488) for 1 h. Fluorescence images were then acquired using CLSM.

Cellular Uptake Study: Caco-2 cells (5×10^4 cells per well) were seeded onto polycarbonate membranes in Transwell chambers (Corning, pore size: 0.4 µm) and cultured for 21 days. The Caco-2 monolayer was washed twice with PBS and equilibrated with pre-warmed HBSS for 30 min. The cells were then incubated with either FITC-INS solution or FITC-INS-loaded nanoparticles at an FITC-INS concentration of 50 µg mL^{-1} for 2 h at 37 °C. Subsequently, the cells were rinsed with PBS, fixed with 4% paraformaldehyde, and stained with DAPI for 10 min. Cellular uptake was then visualized using a confocal laser scanning microscope (CLSM, Zeiss, Germany).

Caco-2 monolayers were incubated with MOP@T@D, 50 µM Tf + MOP@T@D, 50 µM Dc + MOP@T@D, or 50 µM Tf + 50 µM Dc + MOP@T@D at an FITC-INS concentration of 50 µg mL^{-1} for 4 h. The cells were collected and washed twice with PBS, and analyzed for uptake by flow cytometry (FACSCalibur, BD Biosciences, U.S.A.). Then ASBT-mediated endocytosis was next investigated. Caco-2 monolayers were separately incubated with MOP@T and MOP@T@D at an FITC-INS concentration of 50 µg mL^{-1} for 4 h at 37 °C. After three washes with PBS and fixation with 4% paraformaldehyde for 30 min, ASBT was labeled using a goat polyclonal antibody against ASBT (primary antibody) followed by Cy3-conjugated goat anti-rabbit IgG (secondary antibody). Cell monolayers were stained with DAPI. The fluorescence images were acquired by CLSM.

Intracellular Trafficking Study: The intracellular transport pathway of MOP@T@D was investigated by assessing co-localization with lysosomes, endoplasmic reticulum, and Golgi apparatus. For the evaluation of lysosome localization, FITC-labeled nanoparticles (50 µg mL^{-1} FITC-Insulin) were incubated with Caco-2 cells for 0.5 and 2 h, respectively. After being washed three times with PBS, the cells were subsequently incubated with a lysosomal probe (Thermofisher Scientific, USA) for 0.5 h. For evaluation of ER and Golgi localization, nanoparticles were incubated with cells for 4 h, washed with PBS, and stained with ER-Tracker and Golgi-Tracker probes following the manufacturer instructions (Thermofisher Scientific, USA). Fluorescence images were obtained via CLSM. The co-localization coefficients were quantitatively analyzed using Fiji software.

The role of deoxycholic acid in basolateral exocytosis was further examined through IBABP immunofluorescence staining. Caco-2 monolayers were treated with MOP@T and MOP@T@D loaded with FITC-Insulin (50 µg mL^{-1}) for 4 h at 37 °C. Following incubation, the monolayers were blocked for 1 h at room temperature and subsequently incubated with rabbit anti-FABP6 antibody overnight at 4 °C. After three PBS washes, the samples were incubated with Alexa 555-conjugated donkey anti-rabbit IgG for 1 h. Cell monolayers were stained with DAPI. The fluorescence images were observed by CLSM.

Basolateral Release Study: For basolateral release assessment, Caco-2 monolayers were exposed to FITC-Insulin - and RITC-MON-labeled MOP@T@D (equivalent to 50 µg mL^{-1} FITC-Insulin) for 2 h. The basolateral medium was then collected and concentrated using 100 kDa cutoff ultrafiltration devices. Emission spectra were measured with an excitation wavelength of 420 nm. In addition, intact MOP@T@D in the basolateral medium was visualized by TEM.

Animals: Male Sprague–Dawley (SD) rats (190–210 g) were provided by Liaoning Changsheng Biotechnology Co., Ltd. (Benxi, China). Rats were raised in a standard environment (light cycle 12:12, temperature 25 ± 2 °C, humidity 60 ± 10%). All experiments were approved by the Laboratory Animal Ethical and Welfare Committee of Shenyang Pharmaceutical University (No. SYPU-IACUC-S2024-1120-202). All animal experiments were

performed under the Guide for Care and the Animal Management Rules of the Ministry of Health of the People's Republic of China.

Ex Vivo and In Vivo Intestinal Epithelial Absorption: Healthy SD rats (190–210 g) were fasted overnight. Following euthanasia, 100 µL of FITC-insulin-labeled MSP, MOP, MSP@T, MOP@T, MSP@T@D, and MOP@T@D (20 IU mL^{-1}) were injected into corresponding 5 cm intestinal segments (duodenum, jejunum, ileum) and incubated in Krebs–Ringer buffer (5 mL, 37 °C). The apparent permeability coefficient (Papp) was determined by measuring fluorescence intensity in the buffer at predetermined intervals. For in vivo assessment, ileal loops (3 cm) in fasted SD rats were ligated and injected with dual-fluorescent-labeled nanoparticles (FITC-Insulin and Cy5-MON). After 1 h, intestinal cryosections were stained with DAPI and imaged by CLSM.

In Vivo Biodistribution: Healthy rats were orally administered FITC-Insulin-loaded MSP@T, MOP@T, MSP@T@D, and MOP@T@D at an insulin dose of 80 IU kg^{-1}. After 4 h, the animals were euthanized, and major organs (heart, liver, spleen, lungs, and kidneys) were collected. Fluorescence imaging and semi-quantitative analysis of the organs were performed using an IVIS spectroscopy system (Perkin Elmer, USA).

Liver Accumulation and Localization Study: The accumulation of MOP@T@D was investigated in healthy rats and diabetic rats. Animals were orally administered dual-fluorescently labeled MOP@T@D (80 IU kg^{-1} of insulin). After 4 h, livers were collected, rinsed with PBS, and fixed in 4% paraformaldehyde (4 °C, 2 h). Tissue sections (20 µm) were prepared, stained with Hoechst 33 342, and imaged via CLSM.

Furthermore, to assess the precise localization of MOP@T@D within the liver, overnight-fasted healthy rats received FITC-insulin-loaded MOP@T@D (80 IU kg^{-1}) orally. After 4 h, livers were collected, frozen, sectioned, and stained with Hoechst 33 342 and Alexa 555-WGA. CLSM imaging was performed.

Glucose Responsiveness Study in Liver: Diabetes was induced in male Sprague–Dawley rats via intraperitoneal streptozotocin injection (STZ, 35 mg kg^{-1}). T2DM rats were confirmed when fasting glycemia exceeded 11.1 mM after two weeks. To examine the glucose-responsive insulin release, diabetic (abbreviated as D) and healthy (abbreviated as H) rats were divided into two parallel groups. In the first group, diabetic rats received a subcutaneous injection of insulin (3 IU kg^{-1}) to normalize blood glucose. After 1 h, diabetic rats were orally administered MSP@T@D or MOP@T@D, while healthy rats received MOP@T@D (80 IU kg^{-1} of insulin) via oral gavage. The rats were sacrificed at 2 h post-gavage for organ collection. The second group was treated similarly but euthanized 5 h post-gavage, with oral glucose administration (2 g kg^{-1}) 1 h prior to euthanasia. Fluorescence imaging of organs was performed using the IVIS system. The liver fluorescence intensity ratio (5 h/2 h) was determined.

In Vivo Pharmacodynamics and Pharmacokinetics Study: Diabetic rats were randomized into six groups and fasted overnight before an oral gavage with insulin solution, MOP, MOP@T, MSP@T@D, or MOP@T@D (80 IU kg^{-1} of insulin). One group of diabetic rats was subcutaneously injected with insulin (5 IU kg^{-1} of insulin). Besides, 3 h after administration, the rats were orally administered 2 g kg^{-1} glucose solution for the oral glucose tolerance test. Blood glucose and insulin levels were measured using a glucose meter (Sannuo, China) and porcine insulin ELISA kit (Sigma-Aldrich, USA), respectively. Equations (2) and (3) are respectively used for the analysis of pharmacokinetic bioavailability (PA) and bioavailability (F) after oral administration, as follows.

$$PA\ (\%) = \frac{AAC_{oral} \times Dose_{s.c.}}{AAC_{s.c.} \times Dose_{oral}} \times 100\% \quad (2)$$

$$F\ (\%) = \frac{AUC_{oral} \times Dose_{s.c.}}{AUC_{s.c.} \times Dose_{oral}} \times 100\% \quad (3)$$

Overnight-fasted healthy rats were received subcutaneous injections of insulin or MOP@T@D (3 IU kg^{-1}). The blood glucose levels were measured over 4 h post-administration. The low glycemic index (HI) was calculated using Equation (4).

$$HI = (BGL_0 - BGL_{min})\ /T_{min} \quad (4)$$

where, BGL_0 is the initial blood glucose value; BGL_{min} is the lowest blood glucose value; and T_{min} is the time to reach the lowest blood glucose value.

Antioxidant and Anti-Inflammatory Test after Long-Term Administration: Diabetic rats received different formulations and a standard feed every 5 h, thrice daily. Rats were injected subcutaneously with insulin (5 IU kg^{-1} of insulin) or orally MOP, MOP@T, MSP@T@D, and MOP@T@D (80 IU kg^{-1} of insulin) before the first and third meals daily over six consecutive weeks. Meanwhile, diabetic control (DC) and normal control (NC) received daily PBS.

Following the six-week treatment period, a comprehensive series of analyses was performed. Hepatic glycogen was assessed qualitatively and quantitatively via periodic acid-Schiff (PAS) staining and a glycogen detection kit (Abcam, UK), respectively. The enzyme activities of glutathione peroxidase (Gpx), superoxide dismutase (SOD), and the level of malondialdehyde (MDA) were measured with commercially available kits (Beyotime, China). Systemic inflammatory cytokine levels (IL-1β, IL-6, and TNF-α) in plasma were quantified by ELISA (Elabscience, China). The content of $SeCys_2$ was determined using HPLC-ICP-MS. Blood levels of HbA1C, triglycerides (TG), total cholesterol (TC), low-density lipoprotein (LDL), and high-density lipoprotein (HDL) were detected.

To examine the restoration of pancreatic islet function, pancreatic islet tissues from rats were harvested and subjected to immunofluorescence analysis. Mouse anti-insulin and rabbit anti-glucagon antibodies, with Cy3- and Alexa Fluor 488-conjugated secondary antibodies, respectively, were used. The percentage of insulin- and glucagon-stained area was calculated. For insulin content measurement, pancreas tissues were homogenized in acidified ethanol, extracted overnight at 4 °C, and subsequent centrifuged. The insulin content in supernatant was then determined using an insulin ELISA kit (Sigma-Aldrich, USA). Additionally, pancreatic sections from different islets were subjected to H&E staining, followed by quantitative analysis of islet areas.

Two weeks after the end of treatment, blood glucose was continuously recorded in different groups of rats to investigate the different groups. HOMA-IR represented a key homeostatic index of insulin resistance, while HOMA-β estimates β-cell function; calculated using Equations (5) and (6), respectively.

$$HOMA - IR = (C_{FINS} \times C_{FBG})\ /22.5 \quad (5)$$

$$HOMA{-}\beta = (20 \times C_{FINS})\ /\ (C_{FBG} - 3.5) \quad (6)$$

where C_{FINS} is fasting serum insulin concentration (µU mL^{-1}), C_{FBG} is fasting blood glucose concentration (mmol L^{-1}).

Assessment of Insulin Secretion in INS-1 Cells: To evaluate β-cell insulin secretion under oxidative stress, INS-1 cells were pre-incubated for 30 min in low-glucose (5.6 mM) medium. Subsequently, glucose-stimulated insulin secretion was assessed by incubating cells for 1 h in media containing either 5.6- or 16.7 mM concentrations. Combined with palmitic acid treatment to induce oxidative stress, the protective effect of metabolite $SeCys_2$ on insulin secretion of β-cells was investigated. Secreted insulin levels were quantified using a commercial ELISA kit (Sigma-Aldrich, USA).

Western Blot Analysis: Western blot analysis was performed to examine protein expression in both liver and pancreatic tissues. Proteins were extracted from liver tissues and pancreatic islets using RIPA buffer and quantified with a BCA kit (Beyotime, China). Equal amounts of protein (25 µg) were separated by 10% SDS-polyacrylamide gel electrophoresis and subsequently transferred onto polyvinylidene fluoride (PVDF) membranes. After blocking with 5% skim milk in Tris-buffered saline containing 0.1% Tween-20 for 2 h at room temperature, the membranes were incubated overnight at 4 °C with specific primary antibodies. For liver tissues, the primary antibodies included IRS (1:1000), AKT (1:1000), and GSK3-β (1:1000). For pancreatic islets, the primary antibodies include IκBα (1:1000), p-IκBα (1:1000), p65 (1:1000), and p-p65 (1:1000). Following incubation with the corresponding horseradish peroxidase (HRP)-conjugated secondary antibodies for 2 h at room temperature, the protein bands were visualized using an enhanced chemiluminescence detection kit. Band intensities were quantified using ImageJ software (National Institutes of Health, USA).

Quantitative Real-Time PCR: Total RNA was isolated from pancreatic tissue by TRIzol reagent (Invitrogen, USA) and reverse-transcribed into cDNA by a cDNA Reverse Transcription kit (Accurate Biotechnology, China). Quantitative PCR was performed using SYBR Green qPCR Master Mix (Bimake, USA) on a CFX Connect Real-Time PCR Detection System (Bio-rad, USA). β-actin was used as the internal control. Relative expressions of mRNA were calculated by the $2^{-\Delta\Delta CT}$ method. The primer sequences used were as follows: Gpx1-F: ACA-GTC-CAC-CGT-GTA-TGC-CTT-C, Gpx1-R: CTC-TTC-ATT-CTT-GCC-ATT-CTC-CTG; Gpx4-F: TCT-GTGTAA-ATG-GGG-ACG-ATG-C, Gpx4-R: TCT-CTA-TCA-CCT-GGG-GCT-CCT-C; TrxR1-F: CAC-GGA-TGA-GGA-GCA-GAC-CAA-TG, TrxR1-R: CAT-ACA-GCC-TCT-GAG-CCA-GCA-ATC**;** TrxR2-F: GGG-AGG-GCA-GCA-GAA-CTT-TGA-TC, TrxR2-R: TAG-TCA-GCC-ACA-GCC-ACC-TTC-C**;** SelK-F: CAG-GTG-TTA-GAC-AGC-CGG-AAT-CAG, SelK-R: CCC-CGT-AGC-CTC-TTC-TTT-TCT-TCA-C.

Biosafety Evaluation: The in vivo safety profile of nanoparticles was evaluated in healthy SD rats. Rats were injected subcutaneously with insulin (5 IU kg^{-1}) or orally MSP@T@D and MOP@T@D (80 IU kg^{-1} of insulin) twice daily over six weeks. Rats in the control group received daily oral administration of PBS. The selenium content of the main organs before and after MOP@T@D administration was detected by ICP-MS. Serum levels of immunoglobulin M (IgM) and immunoglobulin G (IgG) were measured using ELISA kits (Elabscience, China). The levels of ALT, AST, and CREA were analyzed with an automatic biochemical analyzer (Chemray 240, Rayto, China). Upon completion of the treatment, the rats were euthanized. Major organs, pancreatic islets, and the small intestine of rats were collected for histological examination.

Statistical Analysis: All experiments were performed with at least three independent replicates. Data were presented as mean ± standard deviation (SD), and the Shapiro–Wilk normality test was performed for evaluation of normal distribution. Statistical analyses were conducted using Statistical analyses were performed using GraphPad Prism (version 9.0). For comparisons among multiple groups with homogeneous variances, one-way ANOVA followed by Tukey's post hoc test was applied. Comparisons between two groups were performed using a two-tailed Student's *t*-test, with Welch's correction applied for unequal variances. $*P < 0.05$, $**P < 0.01$, and $***P < 0.001$ were statistically significant, moderately significant, and extremely significant, respectively.

Supporting Information

Supporting Information is available from the Wiley Online Library or from the author.

Acknowledgements

This work was supported by the National Natural Science Foundation of China (Grant Nos. U22A20384, 82204298, and 82172086), National Key R&D Program of China [2020YFE0201700], Frontier Technology Platform Program of Educational Department of Liaoning Province [LJ232410163022], and International Industry Technology Research and Development Program [2025JH2/101900046]. H. Z. acknowledged the Research Project (347897), Solution for Health Profile (336355), InFLAMES Flagship (337531), and "Printed Intelligence Infrastructure (PII-FIRI)" from Research Council of Finland. It was also part of the activities of the Åbo Akademi University Foundation (SÅA) funded Center of Excellence in Research "Materials-driven solutions for combating antimicrobial resistance (MADNESS)".

Open access publishing facilitated by Abo Akademi, as part of the Wiley - FinELib agreement.

Conflict of Interest

The authors declare no conflict of interest.

Data Availability Statement

The data that support the findings of this study are available from the corresponding author upon reasonable request.

Keywords

β-cells protection, diselenide bonds, glucose responsive release, mesoporous organosilicon nanoparticles, oral insulin

Received: July 29, 2025
Revised: November 26, 2025
Published online:

[1] M. Alfatama, *Nat. Nanotechnol.* **2024**, *19*, 424.
[2] T. Yang, A. Wang, D. Nie, W. Fan, X. Jiang, M. Yu, S. Guo, C. Zhu, G. Wei, Y. Gan, *Nat. Commun.* **2022**, *13*, 6649.
[3] N. J. Hunt, G. P. Lockwood, S. J. Heffernan, J. Daymond, M. Ngu, R. K. Narayanan, L. J. Westwood, B. Mohanty, L. Esser, C. C. Williams, Z. Kuncic, P. A. G. McCourt, D. G. L. Couteur, V. C. Cogger, *Nat. Nanotechnol.* **2024**, *19*, 534.
[4] R. K. P. Benninger, V. Kravets, *Nat. Rev. Endocrinol.* **2022**, *18*, 9.
[5] A. C. Anselmo, Y. Gokarn, S. Mitragotri, *Nat. Rev. Drug Discovery* **2019**, *18*, 19.
[6] T. D. Brown, K. A. Whitehead, S. Mitragotri, *Nat. Rev. Mater.* **2020**, *5*, 127.
[7] J. Zhang, X. Wei, W. Liu, Y. Wang, A. R. Kahkoska, X. Zhou, H. Zheng, W. Zhang, T. Sheng, Y. Zhang, Y. Liu, K. Ji, Y. Xu, P. Zhang, J. Xu, J. B. Buse, J. Wang, Z. Gu, *Nat. Biomed. Eng.* **2023**, *8*, 1214.
[8] M. Bohley, J. C. Leroux, *Adv. Sci.* **2024**, *11*, 2400843.
[9] J. Wang, Z. Wang, J. Yu, A. R. Kahkoska, J. B. Buse, Z. Gu, *Adv. Mater.* **2021**, *32*, 1902004.
[10] J. Li, L. Sun, F. Bian, S. J. Pandol, L. Li, *Smart Med.* **2024**, *3*, 20230042.
[11] B. Xie, D. Zeng, M. Yang, Z. Tang, L. He, T. Chen, *ACS Nano* **2023**, *17*, 14053.
[12] Z. He, X. Li, Z. Yang, X. Liu, F. Xie, X. Lv, J. Ni, S. Cheng, Q. Liu, J. Cai, *Chem. Eng. J.* **2024**, *483*, 149168.
[13] Y. Ru, K. Liu, X. Kong, X. Li, X. Shi, H. Chen, *Int. J. Biol. Macromol.* **2020**, *152*, 295.
[14] S. Yu, S. Xian, Z. Ye, I. Pramudya, M. J. Webber, *J. Am. Chem. Soc.* **2021**, *143*, 12578.
[15] Y. Ma, W. Wang, C. Li, F. Han, M. He, Y. Zhong, D. Huang, W. Chen, H. Qian, *Adv. Healthcare Mater.* **2024**, *13*, 2302677.
[16] B. Zou, Z. Xiong, Y. Yu, S. Shi, X. Li, T. Chen, *Adv. Mater.* **2024**, *36*, 2401620.
[17] X. Geng, K. Liu, P. Li, H. Xing, X. Pei, J. Chang, W. Yang, X. Wu, *Chem. Eng. J.* **2024**, *492*, 152176.
[18] J. Peng, F. Chen, Y. Liu, F. Zhang, L. Cao, Q. You, D. Yang, Z. Chang, M. Ge, L. Li, Z. Wang, Q. Mei, D. Shao, M. Chen, W.-F. Dong, *Theranostics* **2022**, *12*, 1756.
[19] D. Shao, F. Zhang, F. Chen, X. Zheng, H. Hu, C. Yang, Z. Tu, Z. Wang, Z. Chang, J. Lu, T. Li, Y. Zhang, L. Chen, K. W. Leong, W.-f. Dong, *Adv. Mater.* **2020**, *32*, 2004385.
[20] Y. Yang, F. Chen, N. Xu, Q. Yao, R. Wang, X. Xie, F. Zhang, Y. He, D. Shao, W.-f. Dong, J. Fan, W. Sun, X. Peng, *Biomaterials* **2022**, *281*, 121368.
[21] C. Zheng, X. Wu, M. Liu, Y. Lan, Q. Liu, E. Cai, Z. Liao, J. Shen, *Smart Med.* **2024**, *3*, 20230047.
[22] J. J. Zou, G. Wei, C. Xiong, Y. Yu, S. Li, L. Hu, S. Ma, J. Tian, *Sci. Adv.* **2022**, *8*, abm4677.
[23] J. Liang, M. Bai, Y. Bi, X. Jian, S. Wang, S. Jiang, Y. Zhao, W. Ma, S. Yin, W. Zhang, *J. Controlled Release* **2025**, *378*, 103.

[24] K. S. Kim, K. Suzuki, H. Cho, Y. S. Youn, Y. H. Bae, *ACS Nano* **2018**, *12*, 8893.
[25] M. Santoni, G. Piccinini, G. Liguori, M. R. Randi, M. Baroncini, L. Milaniet, F. Danesi, *Front. Mol. Biosci.* **2025**, *11*, 1529027.
[26] D. N. Lee, S. B. Yang, S. Kweon, J.-H. Lee, K.-J. Lee, Y. Ryu, D. W. Shin, Y. J. Kim, Y.-K. Lee, J. Park, *Biomaterials* **2024**, *308*, 122539.
[27] D. Yang, D. Liu, H. Deng, J. Zhang, M. Qin, L. Yuan, X. Zou, B. Shao, H. Li, W. Dai, H. Zhang, X. Wang, B. He, X. Tang, Q. Zhang, *ACS Nano* **2019**, *13*, 5058.
[28] B. Ding, Z. Zhu, C. Guo, J. Li, Y. Gan, M. Yu, *Acta Pharm. Sin. B* **2024**, *14*, 2006.
[29] A. Wang, W. Fan, T. Yang, S. He, Y. Yang, M. Yu, L. Fan, Q. Zhu, S. Guo, C. Zhu, Y. Gan, *Adv. Funct. Mater.* **2020**, *30*, 1910168.
[30] J. N. Chu, G. Traverso, *Nat. Rev. Gastroenterol. Hepatol.* **2022**, *19*, 219.
[31] Y. Ma, C. Li, F. Han, Y. Liu, U. E. Hani, Y. Zhong, D. Huang, W. Chen, H. Qian, *Chem. Eng. J.* **2024**, *485*, 150129.
[32] Z. Zhang, D. Zhou, X. Luan, X. Wang, Z. Zhu, W. Luo, J. Yang, S. Tang, Y. Song, *ACS Nano* **2023**, *17*, 9313.
[33] R. Clemen, J. Berner, W. Dethloff, P. Schulan, A. Martinet, K. D. Weltmann, T. von Woedtke, T. Grune, K. Wende, S. Bekeschus, *Redox Biol.* **2024**, *77*, 103372.
[34] W. Tao, D. Liu, Z. Guo, P. Han, Y. Ma, M. Wu, R. Zhang, J. He, *Carbohydr. Polym.* **2025**, *348*, 122790.
[35] Y. Chen, R. Xu, B. Xie, L. Ma, Y. He, H. Liu, T. Chen, *ACS Nano* **2025**, *19*, 18256.
[36] G. Liu, R. Xia, M. Gui, L. Zhang, X. Zhou, J. Xue, Y. Cai, Y. Cao, Y. Xiao, Z. Chen, *ACS Nano* **2024**, *18*, 32932.
[37] C. Liu, W. Wang, H. Lai, Y. Chen, L. Li, H. Li, M. Zhan, T. Chen, W. Cao, X. Li, *Bioact. Mater.* **2024**, *37*, 393.
[38] Q. Huang, Z. Liu, Y. Yang, Y. Yang, T. Huang, Y. Hong, J. Zhang, Q. Chen, T. Zhao, Z. Xiao, X. Gong, Y. Jiang, J. Peng, Y. Nan, K. Ai, *Adv. Sci.* **2023**, *10*, 2300880.
[39] S. Wang, Y. Liu, Q. Sun, B. Zeng, C. Liu, L. Gong, H. Wu, L. Chen, M. Jin, J. Guo, Z. Gao, W. Huang, *Adv. Sci.* **2023**, *10*, 2303167.
[40] M. Keshavarz-Rezaei, A. Hatamian-Zarmi, H. Alvandi, B. E. Hosseinzadeh, Z. B. M. Hosseini, *Biomater. Adv.* **2022**, *140*, 213084.
[41] C. Shi, J. Dawulieti, F. Shi, C. Yang, Q. Qin, L. Wan, H. Hu, M. Sun, L. Ren, Y. Zhao, F. Liu, M. Li, L. Mu, D. Liu, D. Shao, K. W. Leong, J. She, *Sci. Adv.* **2022**, *8*, abj2372.
[42] W. Wang, F. Zhong, D. Wang, Y. Zhao, D. Peng, S. Li, Q. Ning, S. Tang, C.-Y. Yu, H. Wei, *J. Colloid Interface Sci.* **2023**, *646*, 118.
[43] C. Chu, Y. Deng, H. Liu, M. Wei, X. Xu, J. Gou, H. He, T. Yin, Y. Zhang, X. Tang, *Int. J. Pharm.* **2023**, *636*, 122811.
[44] P. Xiao, H. Wang, H. Liu, H. Yuan, C. Guo, Y. Feng, P. Qi, T. Yin, Y. Zhang, H. He, X. Tang, J. Gou, *ACS Nano* **2024**, *18*, 21091.